Competition for dominance within replicating quasispecies during prolonged SARS-CoV-2 infection in an immunocompromised host

Francesca Caccuri,[1] Serena Messali,[1] Daria Bortolotti,[2] Dario Di Silvestre,[3] Antonella De Palma,[3,†] Chiara Cattaneo,[4] Anna Bertelli,[1] Alberto Zani,[1] Maria Milanesi,[5] Marta Giovanetti,[6,7,‡] Giovanni Campisi,[1] Valentina Gentili,[2] Antonella Bugatti,[1] Federica Filippini,[1] Erika Scaltriti,[8] Stefano Pongolini,[8] Alessandra Tucci,[4] Simona Fiorentini,[1] Pasqualina d'Ursi,[9] Massimo Ciccozzi,[10] Pierluigi Mauri,[3,§] Roberta Rizzo,[2] and Arnaldo Caruso[1,*,**]

[1]Section of Microbiology, Department of Molecular and Translational Medicine, University of Brescia, P.le Spedali Civili, 1, Brescia 25123, Italy, [2]Department of Chemical, Pharmaceutical and Agricultural Sciences, University of Ferrara, Via Luigi Borsari, 46, Ferrara 44121, Italy, [3]Proteomic and Metabolomic Laboratory, Institute of Biomedical Technologies, National Research Council (ITB-CNR), Via Fratelli Cervi, 201, Segrate 20054, Italy, [4]Department of Hematology, ASST Spedali Civili di Brescia, P.le Spedali Civili, 1, Brescia 25123, Italy, [5]Section of Experimental Oncology and Immunology, Department of Molecular and Translational Medicine, University of Brescia, V.le Europa, 11, Brescia 25123, Italy, [6]Laboratório de Flavivírus, Instituto Oswaldo Cruz, Fundação Oswaldo Cruz, Av. Brasil, 4365, Manguinhos, Rio de Janeiro 21040-360, Brazil, [7]Laboratório de Genética Celular e Molecular, Instituto de Ciências Biológicas, Universidade Federal de Minas Gerais, Av. Pres. Antônio Carlos, 6627, Pampulha, Belo Horizonte, Minas Gerais 31270-901, Brazil, [8]Risk Analysis and Genomic Epidemiology Unit, Istituto Zooprofilattico Sperimentale della Lombardia e dell'Emilia-Romagna, Str. dei Mercati, 13a, Parma 43126, Italy, [9]Institute of Technologies in Biomedicine, National Research Council, Via Fratelli Cervi, 201, Segrate 20054, Italy and [10]Unit of Medical Statistics and Molecular Epidemiology, University Campus Bio-Medico of Rome, Via Álvaro del Portillo, 21, Rome 00128, Italy

[†]https://orcid.org/0000-0001-5937-8604
[‡]https://orcid.org/0000-0002-5849-7326
[§]https://orcid.org/0000-0003-4364-0393
[**]https://orcid.org/0000-0001-5178-566X
*Corresponding author: E-mail: arnaldo.caruso@unibs.it

Abstract

Severe acute respiratory syndrome coronavirus 2 (SARS-CoV-2) variants of concern (VOCs) emerge for their capability to better adapt to the human host aimed and enhance human-to-human transmission. Mutations in spike largely contributed to adaptation. Viral persistence is a prerequisite for intra-host virus evolution, and this likely occurred in immunocompromised patients who allow intra-host long-term viral replication. The underlying mechanism leading to the emergence of variants during viral persistence in the immuno-compromised host is still unknown. Here, we show the existence of an ensemble of minor mutants in the early biological samples obtained from an immunocompromised patient and their dynamic interplay with the master mutant during a persistent and productive long-term infection. In particular, after 222 days of active viral replication, the original master mutant, named MB61^0, was replaced by a minor quasispecies (MB61^{222}) expressing two critical mutations in spike, namely Q493K and N501T. Isolation of the two viruses allowed us to show that MB61^{222} entry into target cells occurred mainly by the fusion at the plasma membrane (PM), whereas endocytosis characterized the entry mechanism used by MB61^0. Interestingly, coinfection of two human cell lines of different origin with the SARS-CoV-2 isolates highlighted the early and dramatic predominance of MB61^{222} over MB61^0 replication. This finding may be explained by a faster replicative activity of MB61^{222} as compared to MB61^0 as well as by the capability of MB61^{222} to induce peculiar viral RNA-sensing mechanisms leading to an increased production of interferons (IFNs) and, in particular, of IFN-induced transmembrane protein 1 (IFITM1) and IFITM2. Indeed, it has been recently shown that IFITM2 is able to restrict SARS-CoV-2 entry occurring by endocytosis. In this regard, MB61^{222} may escape the antiviral activity of IFITMs by using the PM fusion pathway for entry into the target cell, whereas MB61^0 cannot escape this host antiviral response during MB61^{222} coinfection, since it has endocytosis as the main pathway of entry. Altogether, our data support the evidence of quasispecies fighting for host dominance by taking benefit from the cell machinery to restrict the productive infection of competitors in the viral ensemble. This finding may explain, at least in part, the extraordinary rapid worldwide turnover of VOCs that use the PM fusion pathway to enter into target cells over the original pandemic strain.

Key words: SARS-CoV-2 quasispecies; prolonged infection; viral competition; immunocompromised host; innate immunity; RNA sensing; interferons; proteomic analysis.

1. Introduction

Severe acute respiratory syndrome coronavirus 2 (SARS-CoV-2) emerged in December 2019 in Wuhan, China, and then spread worldwide causing the coronavirus-disease 19 (COVID-19) pandemic (Alteri et al. 2021). In the general population, clinical features of COVID-19 range from asymptomatic to critical illness. However, adult patients with hematologic malignancies and COVID-19 have a worse outcome and high risk of dying

(Passamonti et al. 2020; Vijenthira et al. 2020). In October 2020, the UK faced a rapid rise in positive COVID-19 cases sustained by a new single phylogenetic cluster that led to the identification of a new SARS-CoV-2 lineage, namely Alpha (B.1.1.7), promptly defined as a variant of concern (VOC; ECDC 2020; Challen et al. 2021). Soon after, in South Africa, Brazil, and India, new circulating lineages also defined VOCs were described and designated Beta (B.1.351; Tegally et al. 2021), Gamma (P.1; Faria et al. 2021), and Delta (B.1.617.2; Dhar et al. 2021). In November 2021, the last VOC named Omicron (B.1.1.529) emerged in South Africa (Viana et al. 2022) and it actually starts replacing all other VOCs worldwide and dominating the pandemic scenario.

All VOCs are characterized by a typical mutational pattern in the spike receptor-binding domain (RBD), the most variable part of the coronavirus genome (Wu et al. 2020; Zhou et al. 2020), leading to human angiotensin-converting enzyme 2 (ACE2) increased affinity and consequently, enhanced infectivity (Starr et al. 2020; Nelson et al. 2021). This evidence suggests that viral evolution is ongoing and aimed to adapt to the host and acquire more fitness.

Viral persistence is a prerequisite for intra-host virus evolution (Kang et al. 2020; Zapor 2020). Duration of SARS-CoV-2 shedding through respiratory secretions is highly variable among individuals and is independent of the presence of symptoms (Lee et al. 2020), ranging from a few days to more than 1 month (Cevik et al. 2021). Prolonged detection of viral RNA genome and SARS-CoV-2 positivity have been documented (Choi et al. 2020; Kang et al. 2020) but it is increasingly evident that viral transmission posed by post-convalescent COVID-19 patients may be negligible. For example, in one study of healthcare workers self-isolating due to persistent reverse transcriptase-polymerase chain reaction (RT-PCR) positivity up to 55 days after the onset of symptoms, no viable virus was recoverable in 29 out of 29 nasopharyngeal/oropharyngeal samples tested (Laferl et al. 2021). However, there is no evidence whether these results can be applied to special populations such as immunocompromised patients. Recent reports have, in fact, described cases where the virus can be isolated more than 2 months after its first detection (Avanzato et al. 2020; Choi et al. 2020).

The reasons why some people have productive long-term infection have been not yet completely understood even if this phenomenon has been found to occur in immunocompromised patients only (Camprubí et al. 2020; O'Sullivan et al. 2020; Abdul-Jawad et al. 2021; Baang et al. 2021; Hensley et al. 2021; Siqueira et al. 2021). It has been suggested that the emergence of VOCs worldwide has likely occurred in immunocompromised patients who allowed intra-host persistent infection and variations in viral population (Al Khatib et al. 2020; Avanzato et al. 2020; Choi et al. 2020; Kemp et al. 2020; Lythgoe et al. 2021; Valesano et al. 2021; Wang et al. 2021a, 2021b). Indeed, phylogenetic, population, and computational analyses of viral sequences showed that increased diversity was associated with prolonged viral replication (Voloch et al. 2021). It is worth noting that the RNA virus population in a host is not represented by a single dominating sequence but rather consists of an ensemble of replicating viruses characterized by closely related sequences termed quasispecies (Sun et al. 2021). This allows RNA viruses to have a greater possibility to find the best adapting quasispecies to the specific host, usually achieved by changes in functional genes such as the *S* gene (Zhou et al. 2020). These findings raise the question about the underlying mechanism leading to the emergence of variants during viral persistence in the immunocompromised host.

Here, we describe the case of an immunocompromised patient affected by B-cell lymphoma where the persistent replication of SARS-CoV-2 led to the accumulation of critical amino acid (aa) changes within the spike protein RBD. These mutations occurred early during infection and reflected the dynamic changes of quasispecies through competitive interactions in the viral population, probably aimed to determine a better replicative activity and overcome selective immune responses. Our results provide new insights into the intra-host evolution, highlighting the competition among replicating ensembles for dominance.

2. Materials and methods

2.1 Specimen collection
From 2 April to 28 December 2020, nasopharyngeal swabs (FLOQSwabs COPAN, Brescia, Italy) were periodically collected in a universal transport medium (UTM, COPAN) for diagnostic purposes during hospitalization or at the Brescia community testing site. Samples were transported to the Microbiology Division of the Brescia Civic Hospital (Brescia, Italy). This work was approved by the Brescia Ethical Committee, and the patient provided written consent to publish this case study.

2.2 SARS-CoV-2 detection in nasopharyngeal samples
Nasopharyngeal samples were processed using the InGenius automatic system (ElitechGroup, Turin, Italy), according to the manufacturer's instructions. The presence of SARS-CoV-2 nucleic acid was evaluated using the GeneFinder™ COVID-19 PLUS RealAmp Kit (Osang Healthcare, Anyang-si, Gyeonggi-do, Republic of Korea) whose reagents detect conserved regions in *ORF1ab, E* and *N* genes of the SARS-CoV-2 genome. Cycle threshold (Ct) values and results were automatically calculated by InGenius analysis software.

2.3 Cells
Vero E6 and Caco-2 cell lines were obtained from Istituto Zooprofilattico Sperimentale (Brescia, Italy) and maintained in Dulbecco's Modified Eagle Medium (Gibco, Thermo Fisher Scientific, Waltham, MA, USA) supplemented with 10 per cent fetal bovine serum (FBS; Gibco, Thermo Fisher Scientific).

Calu-3 cell line (HTB-55) was purchased from the American Type Cell Culture Collection (Rockville, MD, USA). Cells were cultured in complete Eagle's minimum essential medium (Gibco, Thermo Fisher Scientific) supplemented with 10 per cent FBS, 1 per cent sodium pyruvate (Gibco, Thermo Fisher Scientific), and 1 per cent L-glutamine (Gibco, Thermo Fisher Scientific). Cells were maintained at 37°C in a humidified atmosphere of 5 per cent CO_2.

2.4 Viral infection
Infection experiments were run as previously described (Caccuri et al. 2020; Caruso et al. 2021) using the clinical SARS-CoV-2 isolates $MB61^0$ and $MB61^{222}$ (Fiorentini et al. 2021). The viruses were propagated in Vero E6 cells, and the viral titer was determined by a standard plaque assay. All the experiments were performed in a biosafety level-3 laboratory using viruses at a multiplicity of infection (MOI) of 0.01. When reported, the cells were infected simultaneously with both $MB61^0$ and $MB61^{222}$ SARS-CoV-2 isolates at an MOI of 0.01 each.

2.5 Growth kinetics of SARS-CoV-2 isolates
Calu-3 and Caco-2 cells were infected in culture media without FBS containing $MB61^0$ and $MB61^{222}$ SARS-CoV-2 isolates at Passage 1, alone or in combination, soon after having confirmed their identity with the original patient's sample by next-generation whole-genome sequencing. After a 1-h incubation at 37°C and

5 per cent CO_2, the inoculum was removed and the cells were washed twice with phosphate-buffered saline (PBS) and replaced with 3 ml of culture media supplemented with 2 per cent FBS. Supernatant samples were taken at 0, 12, 24, 48, 72, and 96 h post-infection (p.i.). The release of the viable virus was evaluated by standard plaque assay and digital droplets polymerase chain reaction (ddPCR).

2.6 Digital droplets polymerase chain reaction

Total RNA was extracted using the QIAamp DSP Virus kit (Qiagen, Hilden, Germany) following the manufacturer's guidelines. ddPCR reaction was carried out on a QX 200 ddPCR system with Automated Droplet Generator (Bio-Rad Laboratories, Hercules, CA, USA) using the One-Step SARS-CoV-2 ddPCR Kit (Bio-Rad Laboratories). Fluorescence of each droplet was evaluated using the QX 200 Droplet Reader (Bio-Rad Laboratories) equipped with Quanta-Soft v1.7 Software. To evaluate the viral load in ddPCR, we used the QuantaSoft Analysis Pro v1.0 Software (Bio-Rad Laboratories) that accompanied the droplet reader to calculate the concentration of the target sequences, along with Poisson-based 95 per cent confidence intervals. The positive populations for each probe are identified using SARS-CoV-2 Standard positive control supplied with the One-Step SARS-CoV-2 ddPCR Kit (Bio-Rad Laboratories). The declared analytic sensitivity of the ddPCR kit is 0.260 cp/μl to 0.351 cp/μl for N1 and N2 probe sets, respectively. The data generated by the QX 200 Droplet Reader were rejected from subsequent analysis if a low number of total droplets was measured in 22 μl PCR (<10,000) or if all of the droplets were positive (saturation of the reaction) (Racki et al. 2014).

2.7 Illumina sequencing

An amplicon-based approach, targeting 343-nucleotide-long partially overlapping subgenomic regions that cover the entire SARS-CoV-2 genome, was used. Total RNA was extracted from 200 μl UTM. Full-length SARS-CoV-2 genomes were then generated using Paragon Genomics' CleanPlex multiplex PCR Research and Surveillance Panel, according to the manufacturer's protocol (Al Khatib et al. 2020; Li et al. 2020; Alteri et al. 2021). Purified library was quantified with Qubit Fluorometer (Qubit DNA HS Assay Kit, Thermo Fisher Scientific). Amplicon library was loaded in a 300-cycle sequencing cartridge, and the deep sequencing was performed on MiSeq platform (Illumina, San Diego, CA, USA). Raw data were checked for quality using FastQC (https://www.bioinformatics.babraham.ac.uk/projects/fastqc/) and then analyzed with the specifically designed software SOPHiA GENETICS' SARS-CoV-2 Panel (SOPHiA GENETICS, Lausanne, Switzerland). To confirm data analyses, the paired-end reads were trimmed with Trimmomatic ver. 0.38 for quality (Q score > 25) and length (>36 bp) and then were analyzed with Geneious® software (version 11.1.5; Biomatters Ltd, Auckland, New Zealand). A consensus sequence was reconstructed by mapping the reads to the SARS-CoV-2 reference sequence NC_045512 using Bowtie2 in sensitive-local mode with consensus threshold at 65 per cent. The variant calling was carried out by the Variant Finder Tool (Geneious) filtering out variants with a P-value greater than 0, using a minimum variant frequency of 0 and default parameters for maximum variant P-value (10^{-6}). To minimize false discoveries, a stringent approach to evaluate the presence of quasispecies spectrum in the patient's samples was applied. An intra-host single nucleotide variant (iSNV) was identified at genome positions with >4,000-fold sequencing coverage and with at least four reads supporting the nucleotide substitution. Amino acid substitutions at the identified iSNV sites were

measured as the proportion of paired-end mapped reads with the alternative amino acid.

2.8 Phylogenetic analysis

We combined the 12 sequential viral consensus genomes obtained from the patient with 2419 sequences available on Global Initiative on Sharing All Influenza Data (GISAID) (https://www.gisaid.org/) and representative of the SARS-CoV-2 lineage B.1.1 globally circulating until November 2021. Only genomes >29,000 bp and <1 per cent of ambiguities were retrieved; low-quality genomes (>10 per cent of ambiguous positions) were excluded. Sequences were aligned using multiple alignment using fast fourier transform (MAFFT) (FF-NS-2 algorithm) employing default parameters (Nakamura et al. 2018). The alignment was manually curated to optimize the number and location of gaps using Aliview (Larrson 2014). Lineage assessment was conducted using the Phylogenetic Assignment of Named Global Outbreak LINeages tool available at https://github.com/hCoV-2019/pangolin (O'Toole et al. 2021). Phylogenetic analysis was performed using the maximum likelihood (ML) method implemented in IQ-TREE2 employing the general time reversible + Γ model model of nucleotide substitution (Minh et al. 2020). The statistical robustness of individual nodes was determined using the Shimodaira–Hasegawa approximate likelihood ratio test branch support. The branches in the ML tree were then converted into units of calendar time in TreeTime (Sagulenko et al. 2018) using a constant rate of 0.0008 substitutions/site/year (Wilkinson et al. 2021) with a clock standard deviation of 0.0004 substitutions/site/year.

2.9 Molecular modeling

The starting structure for the wild-type (WT) human $ACE2_{(hACE2)}$ protein in complex with the SARS-CoV-2 spike protein RBD [Protein Data Bank (PDB) ID 6M0J] was obtained from the research collaboratory for structural bioinformatics PDB. Homology modeling SWISS-MODEL web server was used both for adding missing residue and constructing Q493K-N501T model structures (Waterhouse et al. 2018). The Zinc ion was preserved from the crystal structure. Molecular dynamics (MD) simulations of the two complexes (WT and Q493K-N501T) were performed using Amber18 (Case et al. 2018) package. The ff14SB force field parameters were used for protein. Each complex was solvated in a periodic cubic water box using the TIP3P water model with 12 Å between the solutes and the edges of the box, and then a suitable number of Na^+ and Cl^- ions was added to neutralize the whole systems. Each system was energy minimized with 500 steps of steepest descent followed by 500 steps of conjugate gradient, with positional restraints of 2 kcal/mol A^2 on all protein atoms and with a cut-off for nonbonded interactions of 8 Å; this minimization protocol was done four times. The systems were then subjected to a heating procedure of 25,000 steps, from 0.1 to 300 K in an constant-temperature, constant-volume ensemble with a Langevin thermostat. Bonds involving hydrogen atoms were constrained with the SHAKE algorithm, and 2 fs time step was used. The systems were then equilibrated at 300 K in two consecutive steps of 500 ps each in the constant-temperature, constant-pressure. In the second equilibration step, the positional restraints were removed. MD simulations were performed over 200 ns using the pmemd CUDA program of the Amber18 package and a server Tesla K20 Graphical Processing Unit. The trajectories were analyzed to compare and observe the structural deviation between WT and mutant structures. The conformational ensembles along the last 50 ns of the trajectory were clustered by CPPTRAJ using the hierarchical agglomerative algorithm. Hydrogen bond analyses were carried

out using CPPTRAJ obtaining the hydrogen bond frequency for each residue pair during the MD. In order to identify salt bridge and *van der Waals* interactions of each representative structure, PBePISA web server (Krissinel and Henrick 2007) and RING2.0 web server (Piovesan et al. 2016) were used. Electrostatic potential maps for the WT and mutant structures were calculated using the adaptive Poisson–Boltzmann solver (Jurrus et al. 2018).

2.10 Fusion at the plasma membrane and endocytosis inhibition evaluation

Endocytosis was inhibited by incubation with $25\,\mu M$ chlorpromazine (Sigma-Aldrich, Saint Louis, MO, USA). Cathepsin-mediated proteolysis was prevented by the addition of $20\,\mu M$ Cathepsin L inhibitor III (Calbiochem; Sigma-Aldrich). Plasma membrane (PM) fusion was inhibited by treating with $100\,\mu M$ Camostat Mesylate (Sigma-Aldrich). Calu-3 cell pretreatment was performed by incubating for 1 h at 37°C. Then, media were removed and wells were washed twice with PBS. Untreated and treated cells were then infected. Viral titration was determined by real-time quantitative PCR (qPCR) at 24 and 48 h p.i., as follows. RNA extraction was performed with MagMAX Viral/Pathogen Nuclei Acid Isolation kit (Thermo Fisher Scientific) as previously described (Bortolotti et al. 2020). SARS-CoV-2 titration was obtained by TaqMan 2019nCoV assay kit v1 RealTime-qPCR (Thermo Fisher Scientific).

2.11 Gene expression analysis

RNA sensor pathway genes, cytokines, interferons, IFITMs, and lymphocyte antigen 6E (LY6E) expressions were evaluated on RNA extracted by using the RNeasy kit (Qiagen). DNase treatment was used to check for the presence of contaminant DNA, using β-actin PCR as a control. RT^2 First Strand Kit (Qiagen) was used for RNA reverse transcription, and complementary DNAs were immediately used or stored at −20°C. Gene expression analysis was performed by real-time quantitative PCR using PowerUp SYBR Green Master Mix (Thermo Fisher Scientific) and retinoic acid-inducible gene I (RIG-I) (Hs.PT.58.4273674), *Toll-like receptor 3 (TLR3)* (Hs.PT.25887499.g), TLR7 (Hs.PT.58.39183219.g), *Interferon regulatory factor 3 (IRF3)* (Hs.PT.58.27933933.g), nuclear factor kappa-B (NF-κB) (Hs.PT.58.20344216), *Interleukin (IL)* -1α (Hs.PT.58.40913627), IL-1 (Hs.PT.58.1518186), IL-4 (Hs.PT.58.46539563.g), IL-6 (Hs.PT.58.40226675), tumor necrosis factor (TNF)-α (Hs.PT.58.45380900), IFN-α (Hs.PT.58.24294810.g), IFN-β (Hs.PT.58.39481063.g), IFN-γ (Hs.PT.58.3781960), IFTIM1 (Hs.PT.58.25215635), IFITM2 (Hs.PT.58.1885104.g), IFITM3 (Hs.PT.58.40706345.g), LY6E (Hs.PT.58.22888825.g), or Glyceraldehyde-3-Phosphate Dehydrogenase (Hs.PT.58.25887499.g) PrimeTime qPCR primer assays (Integrated DNA Technologies IDT, Leuven, Belgium).

2.12 RNA sensor pathway analysis

The evaluation of RNA sensors' expression was performed using specific agonists: RIG-I/melanoma differentiation-associated protein 5 (MDA5) agonist 5′-triphosphate hairpin RNA complexed with transfection reagent LyoVec (1 μg/ml; Invivogen, San Diego, CA, USA); TLR3 agonist Poly (I:C) (high molecular weight; 2 μg/ml; Invivogen); and TLR7/8 Agonist–Imidazoquinoline compound R848 (2 μg/ml; Invivogen).

2.13 IRF3, NF-κB expression, and phosphorylation analysis

The evaluation of IRF3 and NF-κB expression and phosphorylation status was performed using the detection kit human total IRF-3 and phospho-IRF-3 (S386) enzyme-linked immunosorbent assay

(ELISA) kit (RayBiotech, Peachtree Corners, GA, USA) and total NF-κB p65 and phospho-NF-κB p65 (S536) (Abcam, Cambridge, UK) on cell lysates.

2.14 Western blot analysis

RIG-I, TLR3, and TLR7 protein expression were quantified by Western blot assay. Whole-cell lysates were treated with radioimmuno-precipitation assay buffer containing proteinase inhibitor cocktail (Sigma-Aldrich). Total proteins were biotinylated with 0.2 mg/ml EZ-Link Sulfo-NHS-LC-Biotin (Pierce, Rockford, IL, USA), immuno-precipitated for 90 min at 4°C with specific monoclonal antibodies (anti-RIG-I, Clone OTI6C1; anti-TLR3, Clone 27N3D4; anti-TLR7, Clone NBP2-24905; and anti-β actin, Clone NB600-501) (Novus Biologics, Centennial, CO, USA), and incubated overnight at 4°C with protein-G Sepharose beads (Santa Cruz Biotechnology, Dallas, TX, USA). The samples were resuspended in 20 μl Laemmli buffer (Bio-Rad). Twenty micrograms of immunoprecipitated proteins were loaded in each well and evaluated in denaturing conditions in 10 per cent TGX precast gel (Bio-Rad), with subsequent electroblotting transfer onto a Polyvinylidene fluoride membrane (Millipore, Burlington, MA, USA). The membrane was incubated with horseradish peroxidase-conjugated streptavidin (Amersham Biosciences, Piscataway, NJ, USA) and developed with the enhanced chemiluminescence kit (Amersham Biosciences). The images were acquired by Geliance 600 (Perkin Elmer, Waltham, MA, USA).

2.15 Quantitative ELISA

IL-1 α, IL-1 β, IL-4, IL-6, IFN-α, IFN-β, and IFN-γ levels were evaluated in cell culture supernatants by single ELISA kit assays (MyBioSource, San Diego, CA, USA) following the customer's protocols.

2.16 Protein extraction and enzymatic digestion

The proteomic analysis described in this study was performed on not infected (NI) Calu-3 cells and on Calu-3 cells infected with SARS-CoV-2 MB61^0 and MB61^{222} isolates, collected at 12, 24, and 48 h p.i. Cells were lysed and proteins were extracted, reduced/alkylated, and enzymatically digested using Easy Pep™ Mini Mass spectrometry (MS) Sample Prep Kit (Thermo Fisher Scientific). Tryptic and Lys-C digestion was carried out in 80 μg of extracted proteins mixture. Following the kit protocol, peptides were generated, cleaned up to prepare detergent-free samples, and resuspended in 0.1 per cent formic acid (Sigma-Aldrich) for liquid chromatography tandem mass spectrometry (LC-MS/MS) analysis in less than 3 h for each examined condition.

2.17 LC-MS/MS analysis

Peptide mixtures were analyzed using Eksigent nanoLC-Ultra® 2D System (Eksigent, part of AB SCIEX Dublin, CA, USA) combined with cHiPLC-nanoflex system (Eksigent) in trap-elute mode. Briefly, for each condition, three technical replicates were performed, injecting 0.8 μg of proteins on the cHiPLC trap (200 μm × 500 μm ChromXP C18-CL, 3 μm, 120 Å, Eksigent, part of AB SCIEX Dublin, CA, USA) and running the loading pump in isocratic mode with 0.1 per cent formic acid in water for 10 min at a flow rate of 3 μl/min. The automatic switching of cHiPLC 10-port valve then eluted the trapped mixture on a nano cHiPLC column (75 μm × 15 cm ChromXP C18-CL, 3 μm, 120 Å, Eksigent, part of AB SCIEX Dublin, CA, USA) through a 132-min gradient of Eluent B (Eluent A, 0.1 per cent formic acid in water; Eluent B, 0.1 per cent formic acid in acetonitrile) at a flow rate of 300 nl/min. In depth, the gradient was from 5 to 10 per cent B in 3 min, 10 to 35 per cent

B in 107 min and 35 to 95 per cent B in 10 min and held at 95 per cent B for 12 min.

The eluted peptides were directly analyzed on an Orbitrap Exploris 120 mass spectrometer (Thermo Fisher Scientific) equipped with EASY-Spray ion source (Thermo Fisher Scientific). Easy spray was achieved using an EASY-Spray Emitter (Thermo Fisher Scientific; nanoflow 7 μm ID Transfer Line 20 μm × 50 cm) held to 1.6 kV, while the ion transfer capillary was held at 220°C. Data-dependent acquisition was performed, acquiring precursor ions in the *m/z* range of 375–1,500 with a resolution (at *m/z* 200) of 60,000 full width at half maximum (FWHM). Precursor fragmentation was carried out at a resolution (at *m/z* 200) of 15,000 FWHM, using higher-energy collisional dissociation method with normalized collision energy of 30 eV and a dynamic exclusion of 20 s. MS and MS/MS data were acquired in profile and centroid mode, respectively, using positive polarity and isotope exclusion. Isolation width was set at 2 *m/z* and first mass was set to 120 *m/z*. Mass spectrometer scan functions and high-performance liquid chromatography solvent gradients were controlled by the Xcalibur data system version 4.4 (Thermo Fisher Scientific) and Eksigent Control Software version 4.3 (Eksigent, part of AB SCIEX Dublin, CA, USA), respectively.

2.18 Data handling

All data generated were searched using the Sequest HT search engine contained in Proteome Discoverer software, version 2.1 (Thermo Fisher Scientific). Experimental MS/MS spectra were compared with the theoretical mass spectra obtained by *in silico* digestion of 29 SARS-CoV-2 protein sequences obtained from UniProt (www.uniprot.org) and *Homo Sapiens* proteome database (74,842 entries), downloaded on March 2021. The following criteria were used for the identification of peptide sequences and related proteins: trypsin and Lys-C as enzymes, methionine oxidation, carbamidomethyl cysteine, three missed cleavages per peptide, and mass tolerances of ±10 ppm for precursor ions and ±0.05 Da for fragment ions. Percolator node was used with a target–decoy strategy to give a final false discovery rate at peptide spectrum match (PSM) level of 0.01 (strict) based on *q*-values, considering maximum deltaCN of 0.05 (Käll et al. 2007). Only peptides with minimum peptide length of six amino acids and Rank 1 were considered. Protein grouping and strict parsimony principle were applied. Results were then exported to an Excel file for further processing.

2.19 Differential expression and network analysis

The 42 LC-MS lists (six runs for the seven available conditions) obtained from the Proteome Discoverer software were aligned, normalized using a total signal normalization method (Griffin et al. 2010), and compared using a label-free quantification approach based on average peptide spectrum matches (aPSMs), as previously reported (Caccuri et al. 2021). Data matrix dimensionality of 5,025 distinct proteins was reduced by linear discriminant analysis (LDA). Following this procedure, we selected and retained proteins with *P* < 0.0001, corresponding to an LDA *F* ratio > 11. Differentially expressed proteins (DEPs) selected by LDA were processed by hierarchical clustering applying the *Ward*'s method and the *Euclidean* distance metric. All processing was performed by JMP15.2 SAS software. Starting from DEPs selected by LDA, pairwise comparisons of cells, infected by the two virus strains and collected at different times p.i., were performed by differential average (DAve) and differential confidence *index* indices (Di Silvestre et al. 2013), and a *H. sapiens* protein–protein interaction

(PPI) network model was reconstructed by STRING Cytoscape App (Doncheva et al. 2019). PPIs were filtered by considering exclusively those 'experiments' or/and 'databases' annotated, with a STRING score ≥ 0.15 and ≥ 0.35, respectively. The reconstructed networks were visualized and analyzed at the functional level by Cytoscape v.3.8.2 and its apps (Su et al. 2014). In particular, DEPs were grouped in functional modules with the support of the *Gene Ontology* enrichment tool inserted in STRING (Doncheva et al. 2019) and BINGO (Maere et al. 2005) Cytoscape apps.

2.20 Statistical analysis

Data were analyzed for statistical significance using the Student's unpaired two-tailed *t*-test or two-way *analysis of variance (ANOVA)* when appropriate. The Bonferroni post-test was used to compare data. Differences were considered significant when *P* < 0.05. Statistical tests were performed using Prism 8 software (GraphPad Software, La Jolla, CA, USA).

3. Results
3.1 Clinical case

On 25 March 2020, a 59-year-old man with a 24-year history of follicular lymphoma was admitted to the hospital for lymphadenopathies, declining edema, and light breathing difficulties. The presence of bilateral pleural effusion, segmental pulmonary embolism, and minimal pericardial effusion suggested the transformation of follicular lymphoma toward an aggressive non-Hodgkin lymphoma. Due to the subsequent development of bilateral interstitial pneumonia and the presence of hypoxemic respiratory failure, on 2 April 2020 (Day 0) the patient was subjected to a nasopharyngeal swab for SARS-CoV-2 testing and was first diagnosed positive for infection. COVID-19-related patient's symptoms required oxygen therapy administered concomitantly with intravenous methylprednisolone and the standard thromboprophylaxis dose of low-molecular-weight heparin. On Day 8, the bone marrow biopsy confirmed the presence of a high-grade large B-cell lymphoma (95 per cent of the bone marrow cells) and, upon the hematological diagnosis, the patient started cyclophosphamide, doxorubicin, vincristine, and prednisone (CHOP) chemotherapy associated with the B-cell depleting monoclonal antibody rituximab (R-CHOP). R-CHOP cycles were well tolerated and administered till Day 53, when he was discharged with no more evident signs of COVID-19. In fact, at that time, he was eupneic and apyretic, with the oxygen saturation within the normal range (97 per cent). Over the course of hospitalization, the patient remained positive for SARS-CoV-2 infection. From Day 53 to 146, he quarantined asymptomatic at home. During this period, viral RNA was clearly detectable in nasopharyngeal swabs collected on Days 116, 125, and 146. Lymphoma evolution called for the need of autologous transplantation, so the patient was hospitalized for the administration of therapy aimed for stem cell collection on Day 146 (cytorabine plus rituximab) and Day 158 (rituximab). As shown in Fig. 1, SARS-CoV-2 has been continuously detected for as long as 222 days. During this period, SARS-CoV-2 RT-PCR showed a median *RdRp* gene Ct of 25.07 (range from 17.8 to 33.3). Starting from Day 237, he tested negative on seven consecutive samplings (last sampling was on Day 270), indicating that SARS-CoV-2 infection was cleared.

To the best of our knowledge, this is the first described case where an immunocompromised symptomatic individual spontaneously recovers from COVID-19 in the absence of antiviral and/or convalescent plasma treatments.
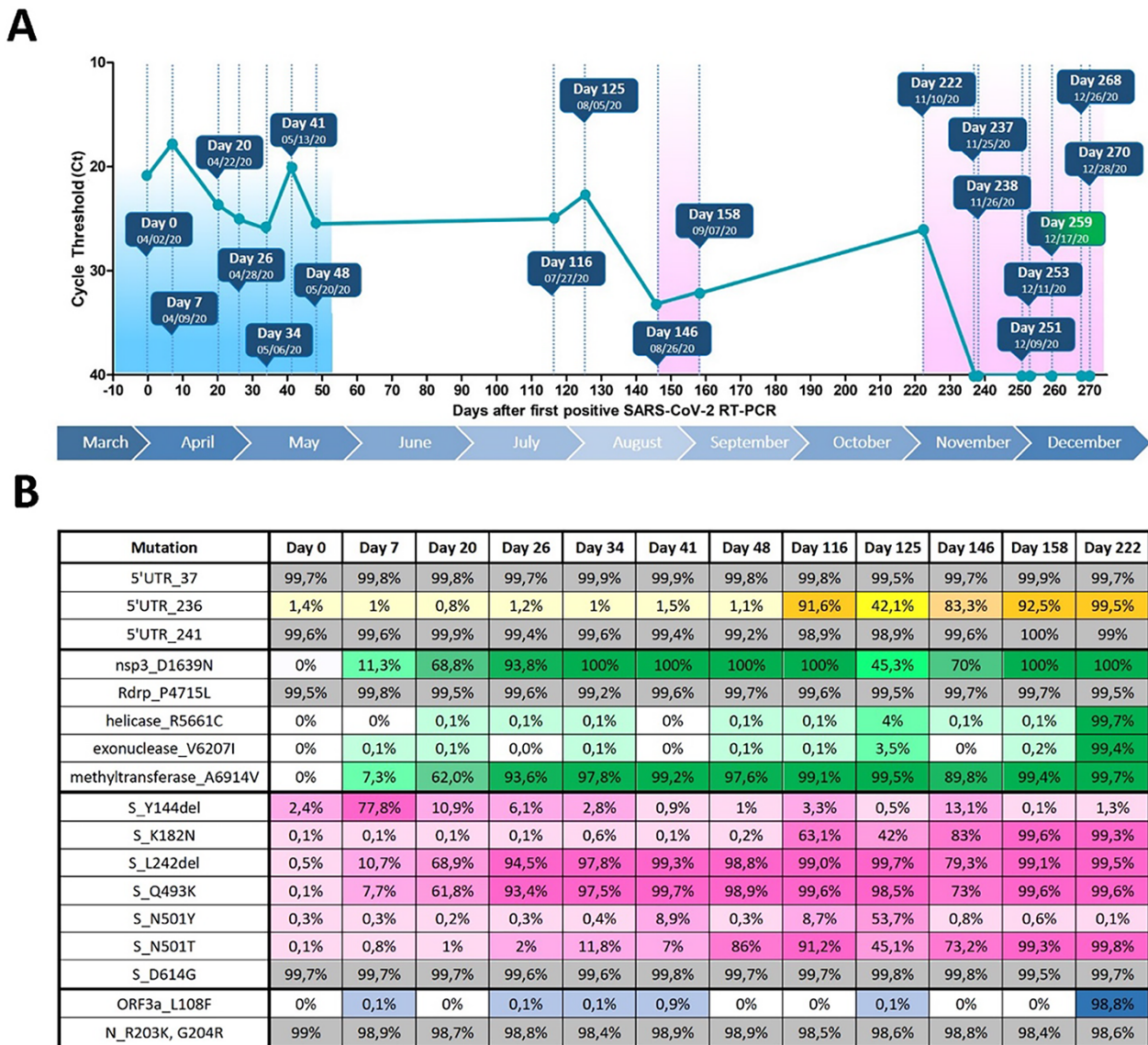
Figure 1. Timeline of SARS-CoV-2 infection and frequencies of longitudinal variants across the SARS-CoV-2 genome in viral quasispecies population. (A) The line graph indicates the SARS-CoV-2 RT-PCR Ct values in nasopharyngeal swabs. Blue boxes highlight the time of sample collection. Green box indicates the time of transplantation. Shaded areas are periods of hospitalization (light blue corresponds to the COVID-19 phase). (B) Table showing the alternative allele frequencies of iSNVs and all amino acid substitutions. To minimize false discoveries, an iSNV was identified at genome positions with >4,000-fold sequencing coverage and with at least four reads supporting the nucleotide substitution. Amino acid substitutions at the identified iSNV sites were measured as the proportion of paired-end mapped reads with the alternative amino acid. Variants types were highlighted in different colors scale. Mutations in gray were in the original Day 0 sample and persisted.

3.2 Intra-host viral genetic diversity

Using deep sequencing data, we were able to follow the dynamics of the intra-host evolution during a prolonged SARS-CoV-2 infection (Supplementary Fig. S1). Genetic screening of all samples revealed 610 iSNVs with allele frequency >10 per cent, with nonsynonymous changes representing 408 (85 per cent) out of 482 iSNVs detected in coding regions. The highest abundance of iSNVs was mainly scattered over *Orf1ab* and *S* genes. In particular, *Orf1ab* harbored the majority of the iSNVs detected ($n = 266$) followed by the *S* ($n = 156$), *N* ($n = 36$), *orf3a* ($n = 21$), *E* ($n = 2$), and *orf8* ($n = 1$) genes and noncoding regions ($n = 128$). The comparison of iSNVs down to low frequencies among serial samples has revealed an elevated accumulation of SARS-CoV-2 intra-host variants emerged out of a population that existed previously. Patterns in the variant frequencies suggest a competition between virus populations carrying different mutations. For example, viruses with the spike deletion [S_Y144del (21991 del-TTA)] rose to high frequency on Day 7 but were then quickly outcompeted by another population without this deletion from Day 20. Many of the iSNVs with a small representation in the early samples appeared with almost the same frequencies also in later samples, suggesting that the competition between the intra-host populations was maintained. Notably, most iSNVs were remarkably stable while others showed a specific trend across sampling dates. For instance, eight iSNVs [5′UTR_236 (236 G->T), nsp3_D1639N (5180 G->A), Rdrp_L5230= (15952 C->T), methyltransferase_A6914V (21005 C->T), S_K182N (22108 A->C), S_L242del (22286 del-CTT), S_Q493K (23039 C->A), and S_N501T (23064 A->C)] showed continuous increase in allele frequency becoming a stable change in the consensus sequence of the last samples. In addition, these iSNVs

with similar growth rates but appearances at different time points confirmed the coexistence of diverse viral populations within each sample.

Concerning nonsynonymous substitutions, genomic analysis of sequences revealed that since Day 26, the virus showed non-conserved amino acid (aa) changes in a number of viral proteins. In particular, one aa mutation was observed in nsp3 (D1639N) and in methyltransferase (A6194V) (Supplementary Fig. S2A). At the same time, we observed the occurrence of one deletion (L242del) and one mutation (Q493K) in the spike S1 region (Supplementary Fig. S2A and S2B). These aa changes were represented in the consensus sequence of all consecutive samples until the infection was cleared. It is worth noting that the Q493K mutation has been rarely found elsewhere up to 15 March 2021, since only 30 out of 784,883 (0.004 per cent) genomes available on GISAID (https://www.gisaid.org/) showed the presence of K at the Spike Position 493. As shown in Supplementary Fig. S2B and in Fig. 1B, an N501T mutation in the spike S1 region, firstly observed in the consensus sequence on Day 48, initially appeared in 11.8 per cent of the total reads on Day 34 and then became predominant in all the subsequent samplings, being maintained till viral clearance. Interestingly, on Day 125, we found that an N501Y sequence transiently dominated over the N501T (53.7 per cent vs. 45.1 per cent, respectively) but disappeared soon after. In the last viremic sample collected on Day 222, other three non-conserved aa substitutions were expressed in helicase (R5661C), exonuclease (V6207I), and orf3a (L108F). The sudden appearance of these nonsynonymous mutations in the master sequence on Day 222 is likely to reflect virus evolution more than the emergence of previously concealed quasispecies.

Surprisingly, all dominant non-conserved aa substitutions or deletions we observed over time, even transiently, in the spike S1 region were already present in nasopharyngeal swabs collected as early as on Days 0 and 7 (Fig. 1B). This finding highlights a fast change also in the genetic characteristics of a key functional gene such as the S gene, further suggesting a dynamic replacement of genome subpopulations of related quasispecies within replicating ensembles.

3.3 Phylogenetic analysis of consensus sequences

In order to understand the evolution of SARS-CoV-2 and the dynamics of iSNVs in an immunocompromised host, we performed a phylogenetic analysis using viral consensus sequences obtained from 12 nasopharyngeal swabs collected between Day 0 and Day 222. The time-stamped tree revealed the phylogenetic relationship among the 12 generated strains and showed that all of them belonged to an ancestral SARS-CoV-2 lineage (B.1.1) (Fig. 2). Our results suggest that sequences on Days 0, 7, and 20 are scattered on different branches of the phylogenetic tree. At the same time, sequences obtained from Days 26 to 222 established an independent cluster. This finding further suggests an intra-host virus evolution, in which genomic diversity is relatively heterogeneous during the early stage of infection, but becomes more homogeneous over time as a consequence of virus adaptation to the immunocompromised host in search for better infectivity or resistance to innate immune responses.

3.4 SARS-CoV-2 quasispecies competition *in vitro*

Replicating ensembles are subjected to episodes of competition. This is mostly due to the biosphere diversity in which viruses are installed and to their need of meeting with unique intracellular environments (Domingo et al. 2021). To test the hypothesis

of a dynamic replacement of SARS-CoV-2 quasispecies due to competition mechanisms *in vivo*, we first isolated the dominant virus from nasopharyngeal swabs collected on Day 0 (MB61^0) and on Day 222 (MB61^{222}) and then tested its capability to replicate in two different human cancer cell lines as lung adenocarcinoma (Calu-3) and colon carcinoma (Caco-2). Quantitation of viral genomes in cell supernatants collected at 12, 24, 48, 72, and 96 h p.i. by ddPCR did show a significant difference in the replication of the two isolates in Calu-3 cells at 12 h p.i., with a faster growing of MB61^{222} than MB61^0 (Fig. 3A). At the same time, a significantly faster replication of MB61^{222} was observed in Caco-2 cells at each time p.i., as compared to MB61^0 (Fig. 3B). Similar results were obtained by plaque assay quantification of viable virus (Supplementary Figs. S3A and S3B). For coinfection experiments, Calu-3 and Caco-2 cells were infected with a mixture of each virus at an MOI of 0.01, and supernatant was collected at different time points for virus quantitation by next-generation sequencing (NGS). To this aim, MB61^{222} was distinguished from MB61^0 for its peculiar Q493K and N501T signatures in the S gene. Viral relative abundance of MB61^{222} in comparison to MB61^0 was determined through the analysis of NGS reads. The percentage of reads carrying the nucleotide substitution characterizing MB61^{222} was evaluated compared to the MB61^0 reads. As shown in Fig. 3C, quantification of RNA released over time shows that viral production is very similar in Calu-3 and Caco-2 cells. These data were also confirmed by plaque assay (Supplementary Fig. S3C). However, as soon as 24 h after coinfection of Calu-3 cells, MB61^{222} replication was significantly increased as compared to MB61^0. Approximately 10 per cent of total virus detected in the supernatant of coinfected cells at the experimental endpoint (96 h) was ascribed to MB61^0, suggesting that MB61^{222} actively replaced its competitor (Fig. 3D). Even more striking results were obtained in coinfection experiments performed in Caco-2 cells. In fact, a significantly higher replication activity of MB61^{222} compared to MB61^0 was evident at as early as 12 h p.i., with MB61^{222} representing approximately 70 per cent of the released virus (Fig. 3E). Results obtained suggest that the capability of MB61^{222} to replace MB61^0 in two different target cell lines might be ascribed to mechanisms of interference able to alter viral population dynamics in coinfected cells.

3.5 MB61^0 and MB61^{222} isolates exploit different cell entry mechanisms

One possible difference in the ability of MB61^0 and MB61^{222} to interact with target cells might be ascribed to the cell entry mechanisms. SARS-CoV-2 might enter target cells via endocytosis or PM fusion pathways in the presence of Transmembrane Serine Protease 2 (TMPRSS2); the proteolytic process of SARS-CoV-2 is completed at the PM, but in its absence the virus is endocytosed and sorted into endolysosomes, from which SARS-CoV-2 enters the cytosol via clathrin and cathepsin L (Jackson et al. 2022). We investigated the entry mechanisms used by MB61^0 and MB61^{222} in Calu-3 cells. We observed that TMPRSS2 inhibition obtained by Camostat was able to significantly reduce both MB61^0 and MB61^{222} replication at 24 h p.i. (Fig. 4A). However, the antiviral effect of Camostat was transient, with the amount of released MB61^0 and MB61^{222} at 48 h p.i. similar in cells treated or not with the drug.

Since SARS-CoV-2 might also use endocytic processes, we performed the inhibition of endocytosis via chlorpromazine and cathepsin L inhibitor III, which block clathrin-mediated endocytosis (Vercauteren et al. 2010) and cathepsin L, respectively. As shown in Fig. 4A, inhibition of the clathrin-dependent early endosome formation significantly reduced MB61^0 replication. At the
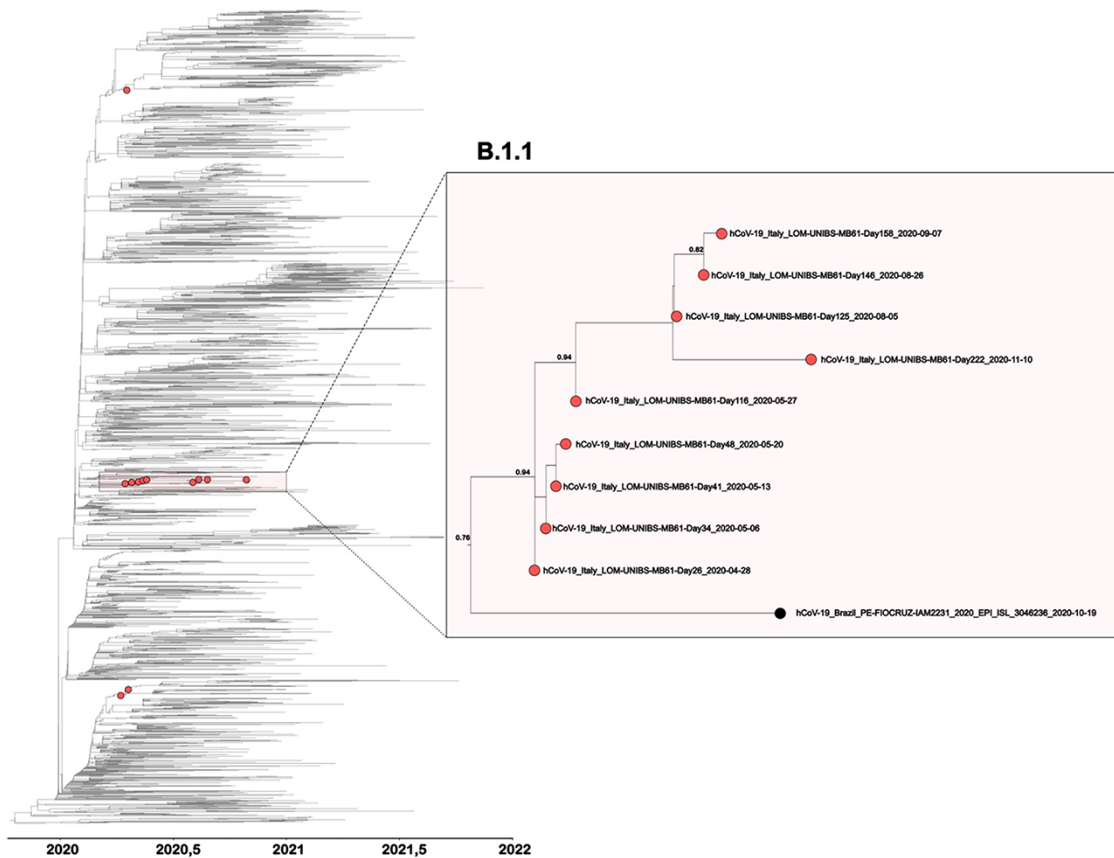
Figure 2. Phylogenetic tree of the B.1.1 isolated sequences. Time-resolved ML tree including the 12 genomes obtained from the immunocompromised patient plus 2,419 sequences representative of the SARS-CoV-2 lineage B.1.1 globally circulating until November 2021. Sequences belonging to the immunocompromised patient are identified by red circles. The clade containing the nine clustering sequences isolated from Days 26 to 222 and their most proximal ancestor sequence (black circle) is highlighted.

same time, cathepsin L significantly reduced MB61[0] replication. On the other hand, clathrin and cathepsin L inhibitors did not exert any effect on MB61[222] replication. These results support a major involvement of the endocytosis entry mechanism for MB61[0], whereas MB61[222] mainly utilizes the PM fusion pathway.

In the effort to elucidate this different behavior of MB61[0] and MB61[222], we evaluated the expression of IFITMs, which are intensely induced during viral infection and play a crucial role in virus restriction of endosomal entry (Winstone et al. 2021). Simultaneously, we evaluated the level of LY6E expression, which is implicated in the control of the PM fusion pathway (Pfaender et al. 2020). As shown in Fig. 4B, MB61[222] infection significantly enhanced the expression of IFITM1 and IFITM2, as compared to MB61[0] infection. At the same time, both isolates did not modify the expression of IFITM3 and LY6E. These results sustain a possible implication of IFITM1 and IFITM2 in the control of endosomal viral entry during SARS-CoV-2 infection. Indeed, MB61[222] mainly uses the PM fusion pathway and escapes this host cell defense mechanism. On the contrary, MB61[0] cannot escape this host antiviral response during MB61[222] coinfection, since it has endocytosis as the main route of entry into the target cell.

3.6 Molecular modeling results

Mutation at Position 501 (N501Y) rose along with the B.1.1.7 variant and is associated primarily with an increase in hACE2 affinity and increased infectivity (Bayarri-Olmos et al. 2021; Liu et al. 2021; Ramanathan et al. 2021; Tian et al. 2021). The role of mutation at Position 493 has been mostly linked to immune evasion (Thomson

et al. 2021). Molecular modeling was then applied to gain better understanding of the role of Q493K and N501T mutations in providing a better interaction with hACE2 and provide a rationale to explain the slightly faster replicative activity of MB61[222] as compared to MB61[0].

Crystal structures of SARS-CoV-2 RBD–hACE2 complex show that the contact regions (CRs) of the RBD are mainly concentrated in the receptor-binding Motif (RBM) denoted as CR1, CR2, and CR3. Q493K and N501T mutations are located in CR2 and CR3, respectively. Protein–protein association between hACE2 receptor and RBD consists of a hydrogen-bonding network and hydrophobic interactions. MD of binary complexes of the RBD with hACE2 was carried out to investigate whether mutations can influence the interfacial interactions. Root-mean-square deviation was assessed during the 200 ns of MD simulation runs for RBD and RBM of SARS-CoV-2 (WT) and SARS-CoV-2 (Q493K + N501T) (mutant; Mut) systems. As shown in Supplementary Fig. S4, there were no significant differences between SARS-CoV-2 WT and Mut in the RBD, RBM, hACE2, and the CRs (H1, H2, H18, and b-turn) of hACE2 during the simulations, thus indicating stable MD simulations for both spikes in these regions. Also, the root-mean-square fluctuation values of hACE2 and the RBD domain of CA atoms in both SARS-CoV-2 WT and Mut complexes were comparable and showed limited fluctuations.

Comparison of the key interfacial interactions between hACE2 and the RBD of SARS-CoV-2 shows that SARS-CoV-2 WT (Fig. 5A) and SARS-CoV-2 Mut (Fig. 5B) have diverse epitope features. In the SARS-CoV-2 Mut RBD–hACE2 the replacement of Q493K maintains
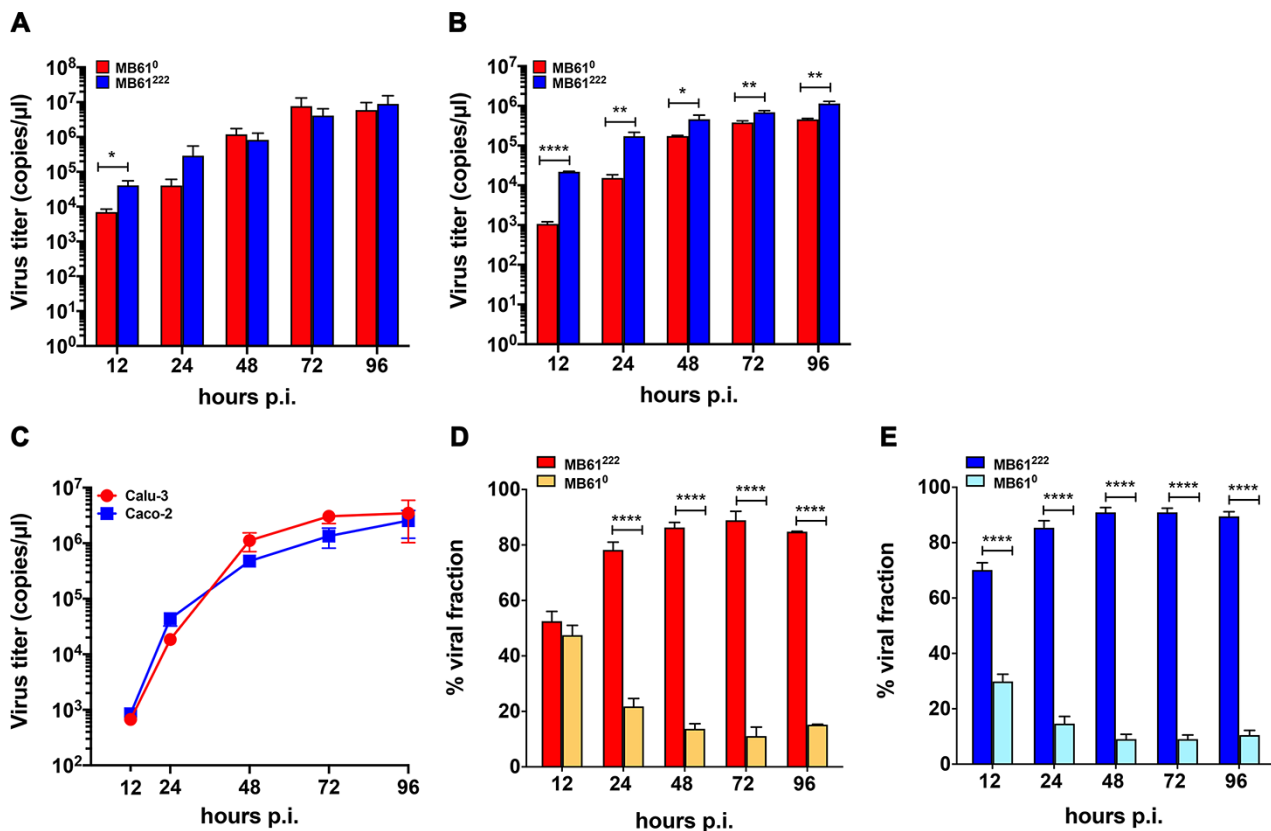
Figure 3. Growth kinetics of the MB61^0 and MB61^{222} patient's isolates in Calu-3 and Caco-2 cell lines. (A) Human lung epithelial cell line Calu-3 and (B) Human colorectal adenocarcinoma cell line Caco-2 cells were infected with MB61^0 or MB61^{222} at an MOI of 0.01. Supernatants from infected cells were harvested at designated time points for assessment of virus titer by ddPCR. Data shown are the mean and the standard error of the mean for three independent replicates. Student's unpaired two-tailed *t*-test was used to determine statistical significance for each time point (*$P < 0.05$, **$P < 0.01$, ****$P < 0.0001$). (C–E) *In vitro* simultaneous coinfection of Calu-3 and Caco-2 cell lines with MB61^0 and MB61^{222}. Calu-3 and Caco-2 cell lines were inoculated simultaneously with the MB61^0 and MB61^{222} patient's isolates at an MOI of 0.01 each. (C) Supernatants from infected cells were harvested at designated time points for assessment of virus titer by ddPCR. Data shown are the mean and the standard error of the mean for three independent replicates. The statistical analysis was performed using a two-way ANOVA, and Bonferroni's post-test was used to compare data. No significant difference in virus titer was observed between the two cell lines at any of the checked time points. Supernatants from infected Calu-3 (D) or Caco-2 (E) cells were collected at designated time points and then subjected to whole-genome sequencing. Graphs show the percentage of MB61^{222} versus percentage of MB61^0 at each of the time points (percentage viral fraction). The percentage of the viral fraction was defined as the number of reads endowing the specific signatures of the MB61^{222} patient's isolate. Data shown are the mean and the standard deviation for two replicates. The statistical analysis was performed using a two-way ANOVA, and Bonferroni's post-test was used to compare data (****$P < 0.0001$).

the hydrogen bond between Residue 493 of CR2 and E35 of hACE2 as in the WT, but the greater flexibility of the lysine side chain compared to glutamine generates a new hydrogen bond between 493K and D38 of hACE2. The new hydrogen bond removes D38 from the delicate hydrogen bond network of CR3 and induces a rearrangement of the interactions in this CR. The replacement of N501T generates a loss of six hydrogen bonds in CR3, but a new hydrophobic patch is generated among T500, V503 of CR3 and Q325, and N330 of hACE2, and these new interactions extend the terminal CR of CR3 by engaging the helix 18 (H18) close to the beta strands of hACE2 (Fig. 5B).

The hydrogen networks observed in the representative conformations obtained from the MD are in agreement with the frequency of the hydrogen bonds calculated during the simulation (Supplementary Fig. S5). Furthermore, Q493K substitution inserts a positive charge, and the lysine forms two new saline bridges among K493 of RBD and E35 and D38 of hACE2. A comparison of the surface electrostatic potential identifies a positively charged patch on the SARS-CoV-2 Mut RBD–hACE2 that is absent on the SARS-CoV-2 WT RBD–hACE2 (Fig. 5C and 5D). K493 contributes to forming positive electrostatic surface in the SARS-CoV-2 Mut

(Fig. 5D). The present study reveals a reorganization of key interfacial interactions between hACE2 and the SARS-CoV-2 Mut RBD. In addition, Q493K conversion in the SARS-CoV-2 Mut RBD creates a positive electrostatic patch that results in greater electrostatic complementarity than that of the SARS-CoV-2 complex.

3.7 MB61^0 and MB61^{222} induce peculiar RNA sensor pathway activation

A differential pathway for viral entry might induce substantial differences in viral RNA sensing by the infected cells since the different timing and localization for genome released engage different intracellular RNA sensors.

We investigated both cytosolic (RIG-I and MDA5) and endosomal (TLR3, TLR7, and TLR8) RNA sensors to identify possible differences between MB61^0 and MB61^{222} SARS-CoV-2 isolates. As shown in Fig. 6, the cytosolic RIG-I RNA sensor was significantly upmodulated as mRNA (Fig. 6A) and protein (Fig. 6B) expression by MB61^{222} only. The endosomal TLR3 and TLR7 RNA sensors were triggered at the mRNA (Fig. 6A) and protein (Fig. 6B) levels by both MB61^0 and MB61^{222}. Interestingly, MB61^{222} induced a
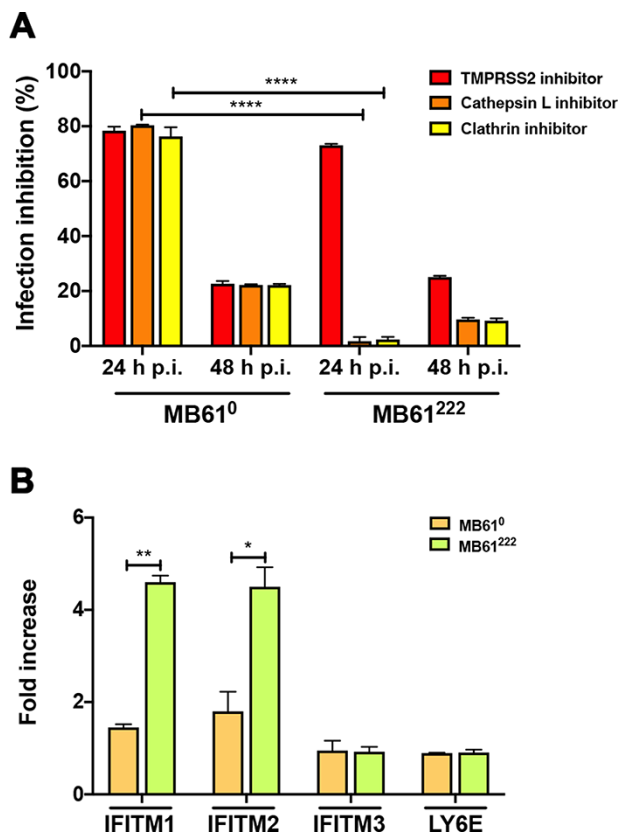
Figure 4. MB61[0] and MB61[222] use different pathways to enter into Calu-3 cells. (A) Calu-3 cells were infected with MB61[0] or MB61[222] at an MOI of 0.01 and treated with TMPRSS2, clathrin, or cathepsin L inhibitors. Data shown are the mean and the standard deviation of the mean for three independent experiments. Student's unpaired two-tailed t-test was used to determine statistical significance between the two isolates for each inhibitor (****$P < 0.0001$). (B) Gene expression of selected SARS-CoV-2 entry factors IFITM1, IFITM2, and IFITM3 and LY6E in Calu-3 cells infected with MB61[0] or MB61[222]. Gene expression was determined by quantitative real-time PCR and normalized to NI Calu-3 cells. Data shown are the mean and the standard deviation of the mean for three independent experiments. Student's unpaired two-tailed t-test was used to determine statistical significance between the two isolates for each inhibitor (*$P < 0.05$; **$P < 0.01$).

higher upmodulation of TLR7 than MB61[0]. On the contrary, MDA5 and TLR8 were not induced by both SARS-CoV-2 isolates. These data suggest that MB61[222] infection induces the transcription and transduction of the cytosolic RIG-I RNA sensor and of TLR3 and TLR7 endosomal RNA sensors. On the contrary, MB61[0] infection enhances TLR3 and TLR7 endosomal RNA sensors only, the latter at a lower extent as compared to MB61[222].

The ability of MB61[222] to engage cytosolic RIG-I RNA sensor suggests a differential downstream transduction as compared to MB61[0] that enhances endosomal TLR3 and TLR7 RNA sensors only. Among the transcriptional factors involved in RNA sensing by viral infected cells, IRF3 and NF-κB play a central role (Schmitz et al. 2014). In particular, IRF3 protein is involved in the production of IFNs (Yanai et al. 2018), whereas NF-κB is mainly employed in the induction of the proinflammatory response (Liu et al. 2017). Even if both IRF3 and NF-κB are reported to be crucial in RNA-sensing signaling, they are differentially induced by different RNA sensors. In fact, while endosomal RNA sensor activation leads mainly to NF-κB recruitment, the cytosolic RNA sensor RIG-1 typically activates both NF-κB and IRF3 signals (Nguyen et al.

2020). As shown in Fig. 6C, significant activation of IRF3 and NF-κB was observed in MB61[222]-infected cells. On the other hand, MB61[0]-infected cells showed an enhanced NF-κB transcription only. These data agree with the differential RNA sensor induction by the two SARS-CoV-2 isolates. MB61[222] was found to significantly enhance RIG-I, TLR3, and TLR7 RNA sensors and consequently both IRF3 and NF-kB transcription and phosphorylation (Fig. 6D). On the contrary, MB61[0] induces TLR3 and TLR7 RNA sensors and the downstream factor NF-kB transcription and phosphorylation (Fig. 6D).

3.8 MB61[0] and MB61[222] SARS-CoV-2 infection triggers different mediators of the innate immune response

It is known that depending on the ability of the cell to sense the presence of an infection, different soluble factors, such as cytokines and IFNs, are released. NF-κB and IRF3 are essential to mediate antiviral actions through the expression of virus-induced and IFN-stimulated genes. We analyzed the expression levels of cytokines, type-I (IFN-α and IFN-β) and type-II (INF-γ) IFNs in Calu-3 cells infected with MB61[0] or MB61[222].

As reported in Fig. 6E, MB61[222] infection significantly increased the mRNA transcription of the proinflammatory cytokines IL-1β and IL-6 in comparison with uninfected and MB61[0]-infected Calu-3. Similarly, IL-1β and IL-6 as well as TNF-α secretion were significantly increased in MB61[222] but not in MB61[0]-infected cells (Fig. 6F). IFN-α, IFN-β, and IFN-γ were significantly induced during MB61[222] infection as mRNA transcription (Fig. 6G) and protein secretion (Fig. 6H) as compared to MB61[0]-infected cells. On the contrary, MB61[0] infection was not found to affect IFN-α and IFN-β transcription and secretion (Fig. 6G and 6H). However, MB61[0] infection was found to significantly induce IFN-γ secretion as compared to uninfected cells (Fig. 6H). These results are in agreement with the differential effects that the two isolates promote on RNA sensors.

Altogether, our results show that MB61[222] enters the target cell via both PM fusion and endocytosis, enhancing cytosolic (RIG-I) and endosomal (TLR3 and TLR7) RNA sensors. The consequent phosphorylation of both IRF3 and NF-κB transcription factors induces the secretion of proinflammatory cytokines (IL-1β, IL-6, and TNF-α) and IFNs (IFN-α, -β, and -γ), under RIG-I and TLRs control. On the contrary, MB61[0] enters the target cell via endocytosis, inducing TLR7 and TLR3 RNA sensors, with the consequent activation of NF-κB and IFN-γ secretion.

3.9 Proteome analysis of SARS-CoV-2-infected Calu-3 cells

Proteomics profiles of Calu-3 cells infected or not with MB61[0] or MB61[222], collected at 12, 24, and 48 h p.i., were analyzed. Through a shotgun label-free platform, based on the coupling of nanoliquid chromatography and high-resolution mass spectrometry (nLC-hrMS/MS), 42 proteomics runs were acquired from the seven examined conditions. A total of 5,113 distinct proteins were identified (Supplementary Table S1), with at least one unique peptide, molecular weights ranging from 2 to 3990 kDa, and isoelectric points ranging from 3.8 to 12.3. The alignment of all protein lists obtained was carried out on the basis of identified proteins and related PSM values, which represent the number of mass spectra attributed to them and indirectly their abundance in the samples. Then, for each experimental condition, three lists were created normalizing and averaging the PSM (aPSMs) values of the proteins identified with high confidence with at least one unique peptide using a total signal normalization method. The LDA was applied
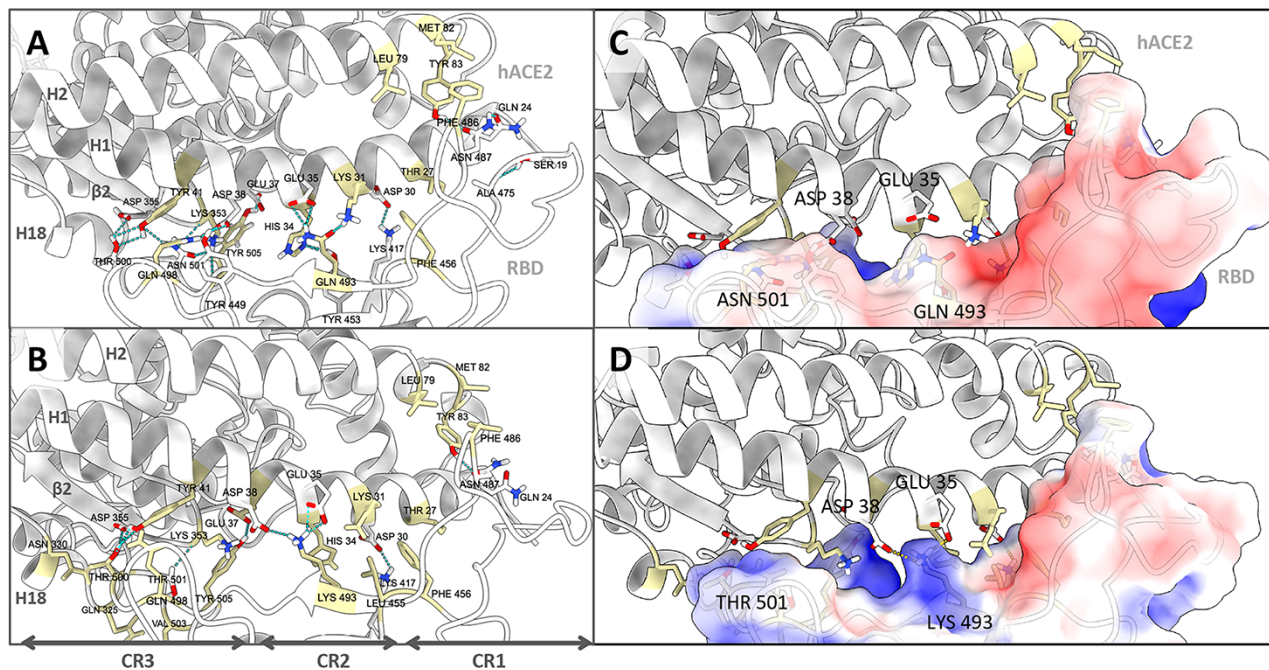
Figure 5. Spike RBM CRs with hACE2 and surface electrostatic potential introduced by the Q493K and N501T mutations. RBM–hACE2 complex and the three CRs at the N-terminal end of hACE2 (CR1), the central region (CR2) of RBM, and the β-turn CR of hACE2 (CR3) are shown. The key interfacial interactions between hACE2 and the RBM of SARS-CoV-2 WT (A) and SARS-CoV-2 Mut RBD (B) in the three CRs are shown. Key hydrogen bonds are highlighted with dashed lines, and hydrophobic contacts are shaded in yellow. Electrostatic interactions of SARS-CoV-2 WT RBD–hACE2 (C) and SARS-CoV-2 Mut RBD–hACE2 (D). Salt bridge is shown in yellow dot line, hydrophobic interactions are shaded in yellow sticks, and electrostatic potential maps are colored in blue to indicate positive potential and red for negative potential.

using the proteomics lists, and 431 statistically significant proteins presenting a *P*-value ≤ 0.0001 were extracted as DEPs (Supplementary Table S2). As shown in Fig. 7A, a clear separation and a different behavior between Calu-3 and MB61[0] or MB61[222]-infected cells, which generate two main branches, were appreciable by the distribution of heatmap colors. A further subgrouping is also evident according to the time p.i. and to the isolate considered. Of note, Calu-3 cells infected with MB61[222] and collected at 48 h p.i. are strikingly different from all the other examined conditions.

Selected DEPs were combined with the *H. sapiens* PPI network to highlight molecular functions and biological processes and pathways affected by virus infection, at different time. Following this strategy, a network model of 421 proteins connected by 4,509 interactions was built. Globally, these proteins were grouped across 51 functional modules (Supplementary Fig. S6). The evaluation of the protein pathways showed a differential induction by the two isolates, supporting our results. In particular, as shown in Fig. 7B, MB61[222] induced RNA-sensing proteins (IFIT1, IFIT2, and IFI16) by MB61[222] (Vladimer et al. 2014) as well as IFN-induced genes (IFI44L, Radical S-Adenosyl Methionine Domain Containing 2, 2′-5′-Oligoadenylate Synthetase 2, 2′-5′-Oligoadenylate Synthetase Like, MX dynamin like GTPase 1, and signal transducer and activator of transcription 1 (STAT1)). The ability of MB61[222] to counteract this host antiviral response might be, at least in part, sustained by the induction of the following: (1) CD59 (Wei et al. 2017), a negative regulator of the terminal pathway of the complement system by binding to the C8/C9 factors; (2) granulin, which binds directly to tumor necrosis factor receptors (TNFRs) and disturbs the TNF-α–TNFR interaction (Tang et al. 2011); (3) Schlafen family member 5 (SLFN5), which represses IFN-induced STAT1 transcriptional activity (Arslan 2017); and (4) nucleobindin 1, which has been shown to inhibit activating transcription factor 6 activity

(Madden et al. 2019). On the contrary, MB61[0] was not found to promote the synthesis of proteins with antiviral activity.

The enhanced endocytic activity during MB61[0] infection is supported by the upmodulation of Huntingtin interacting protein 1 related (HIP1R) (Chen and Brodsky 2005) and Clathrin Interactor 1 (CLINT1), which interact with clathrin, and Glutamine Amidotransferase Class 1 Domain Containing 1 (GATD1) and insulin like growth factor 2 receptor (IGF2R), implicated in intracellular trafficking, and by the focal adhesion proteins (Mucin-5AC (MUC5AC), Talin 1 (TLN1), Laminin Subunit Gamma 2 (LAMC2), Laminin Subunit Beta 3 (LAMB3), four and a half LIM domains 2 (FHL2), and Golgi glycoprotein 1(GLG1)) that might facilitate SARS-CoV-2 adhesion and integrin signaling, which terminates with endosomal trafficking. To facilitate particle uncoating, MB61[0] induced microtubule associated protein RP/EB family member 2, Nuclear Mitotic Apparatus Protein 1, and microtubule actin crosslinking factor 1 that sustain the microtubule-associated particle uncoating. The decreased PM fusion pathway during MB61[0] infection might also be determined by the increased expression of serpin family B member 1 (SERPINB1) by infected cells, which is predicted to reduce the ability of TMPRSS2 to facilitate SARS-CoV-2 entry into airway epithelial cells (Stanton 2020). Interestingly, MB61[0] also enhanced the expression of proteins (GDP dissociation inhibitor 1, *SEC22 Homolog B, Vesicle Trafficking Protein, COPI coat complex subunit gamma 1*, hook microtubule tethering protein 1, ADP ribosylation factor interacting protein 1, ER membrane protein complex subunit 1, ribosome binding protein 1, and signal recognition particle 68) involved in the formation of endoplasmic reticulum-derived perinuclear interconnected membrane structures that contain double-membrane vesicles (DMVs), in which SARS-CoV-2 RNA synthesis occurs (Snijder et al. 2020). The use of endocytosis also by MB61[222] is supported by the expression of
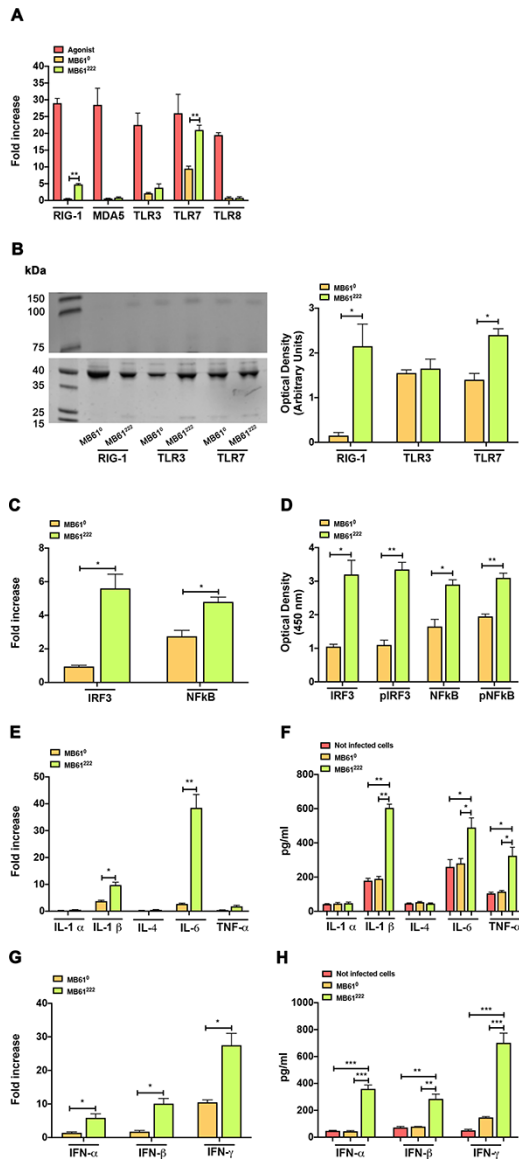
Figure 6. RNA sensors in Calu-3 cells following MB61[0] or MB61[222] infection. (A) Calu-3 cells were infected with MB61[0] or MB61[222] at an MOI of 0.01 for 1 h at 37°C. Thereafter, the cells were washed and cultured for 48 h. Levels of expression of RIG-1, MAD5, TLR3, TLR7, and TLR8 were quantified as fold increases in comparison with NI cells. (B, left panel) Western blot analysis of RIG-I, TLR3, TLR7, and β-actin in Calu-3 infected with MB61[0] or MB61[222] at an MOI of 0.01. The molecular weights were determined by protein ladder. RIG-I, TLR3, and TLR7 were evidenced at 100–116 kDa and β-actin at 44 kDa. (B, right panel) Evaluation of protein expression by densitometry, normalized on β-actin content. (C) Levels of NF-κB and IRF3 expression in MB61[0] or MB61[222]-infected Calu-3 cells in comparison with NI cells. (D) Levels of total and phosphorylated IRF3 and NF-κB in Calu-3 cells infected with MB61[0] or MB61[222] isolates and analyzed 48 h p.i. Levels of (E) mRNA transcription and (F) protein expression of cytokines (IL-1α, IL-1β, IL-4, IL-6, and TNF-α) are reported at 48 h p.i. The amount of cytokines at 24 h p.i. was under the detection limit of the assays. Levels of (G) mRNA transcription and (H) protein expression of IFN-α, IFN-β, and IFN-γ are reported at 48 h p.i. The amount of IFNs at 24 h p.i. was under the detection limit of the assays. Data shown are the mean and the standard deviation of the mean for three independent experiments. The statistical analysis was performed using the Student's unpaired two-tailed t-test (*$P < 0.05$; **$P < 0.01$; ***$P < 0.001$).

actin related protein 2/3 complex subunit 1B (ARPC1B), testin LIM domain protein (TES), and Gc-globulin (GC), which facilitate cargo

enrichment and budding from the endosomal membrane to generate recycling vesicles. It is worth noting that MB61[222] may require this process for receptor recycling (Al-Saleem et al. 2019). Alternatively, the increased expression of dynein light chain LC8-type 2, which controls retrograde vesicle transport, may facilitate virus trafficking to replication sites or may serve to deliver cargoes to replication sites. The formation of DMVs during MB61[222] infection is also supported by the induction of receptor accessory protein 5, which interacts with SARS-CoV-2 structural M protein and plays a crucial role in viral morphogenesis.

4. Discussion

Quasispecies provide an advantage to SARS-CoV-2 for achieving the best fitness during prolonged intra-host evolution by changing the genetic characteristics of key functional genes. Our data show the existence of an ensemble of minor mutants in the early biological samples obtained from an immunocompromised patient and their dynamic interplay with the master mutant during a persistent and productive long-term infection. After 222 days of active viral replication *in vivo*, we highlighted the replacement of the original master mutant by a minor mutant, namely MB61[222], expressing two critical mutations in spike, namely Q493K and N501T. This mutated spike shows a greater affinity to ACE2 than the original spike, which may explain the acquired capability of MB61[222] to gain access into target cells mainly by the PM fusion pathway than endocytosis, which characterizes the entry mechanism used by the previous master mutant named MB61[0]. In this shifting in the entry route preference, we cannot exclude the role played by other spike mutations acquired by MB61[222] during that time. The enhanced endocytic activity during MB61[0] infection is supported by the upmodulation of HIP1R (Chen and Brodsky 2005) and CLINT1, which interact with clathrin, GATD1, and IGF2R, implicated in intracellular trafficking and by the focal adhesion proteins (MUC5AC, TLN1, LAMC2, LAMB3, FHL2, and GLG1) that might facilitate MB61[0] adhesion and integrin signaling, which terminates with endosomal trafficking. On the contrary, the decreased PM fusion pathway during MB61[0] infection might be determined by the increased expression of SERPINB1 by infected cells, which is predicted to reduce the ability of TMPRSS2 to facilitate SARS-CoV-2 entry into airway epithelial cells (Stanton 2020). These findings, in agreement with previous observations (Starr et al. 2020; Nelson et al. 2021), may support the significant increase in infectivity and replication of MB61[222] as compared to MB61[0] we observed at an early time (12–24 h) p.i. It is worth noting that the expression of ARPC1B, TES, and GC, which facilitate cargo enrichment and budding from the endosomal membrane to generate recycling vesicles, might facilitate ACE2 receptor recycling and further contribute to enhancing MB61[222] infectivity (Al-Saleem et al. 2019).

Different modalities of SARS-CoV-2 entry are known to induce the activation of different RNA sensors (Bortolotti et al. 2021; Mdkhana et al. 2021). The ability of MB61[222] to engage cytosolic RIG-I RNA sensor leads to a differential downstream transduction as compared to MB61[0], which enhances endosomal TLR3 and TLR7 RNA sensors only. Consequently, IFN-α, IFN-β, and different proinflammatory proteins are significantly induced during MB61[222] infection. On the contrary, MB61[0] infection did not significantly promote any activation of the innate immune system but INF-γ transcription and secretion only.

In a recent study, Thorne et al. (2021) revealed that mutations outside S gene, including noncoding changes, are important in SARS-CoV-2 adaptation through enhanced innate immune
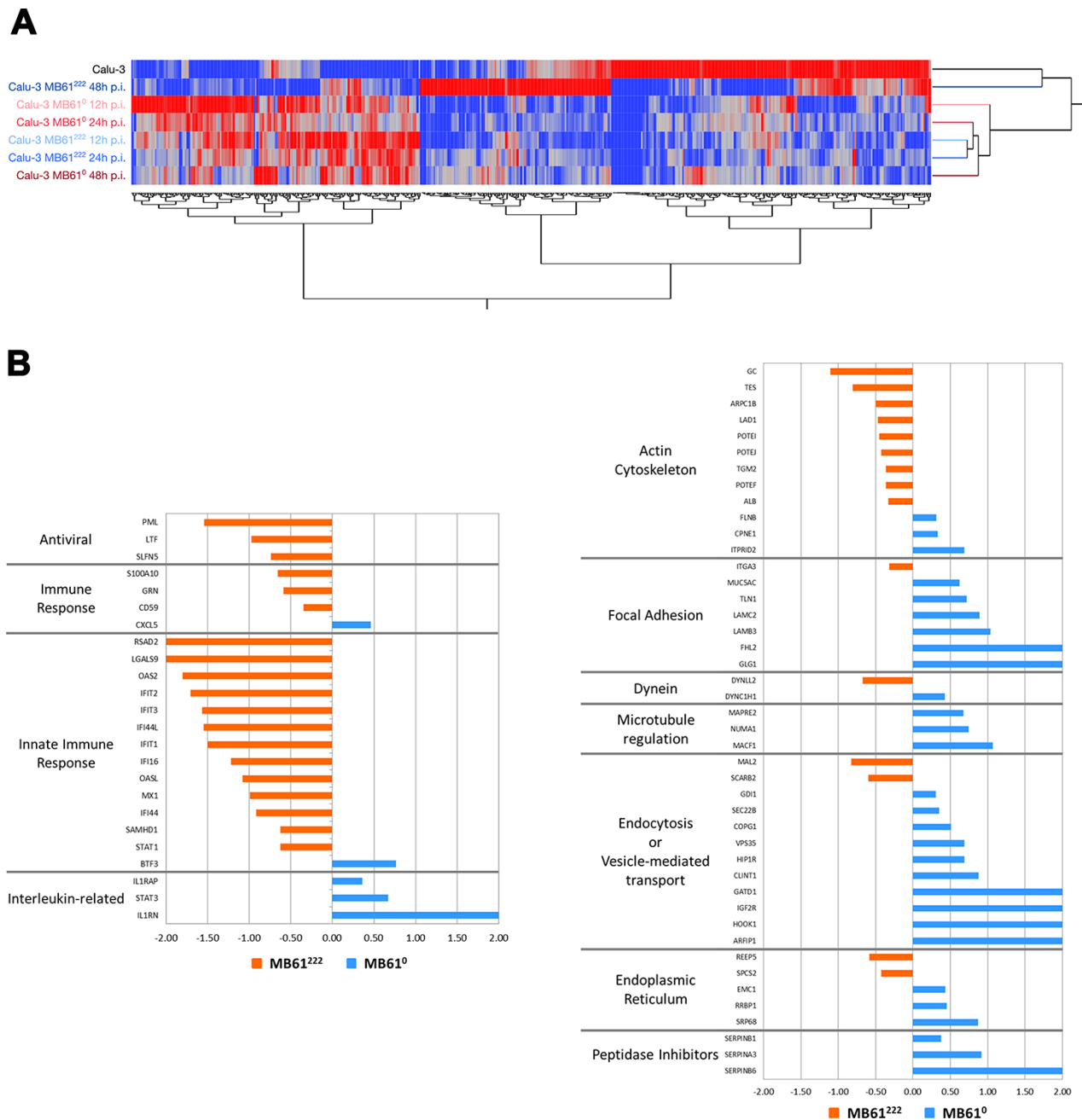
Figure 7. Proteomic analysis of Calu-3 cells infected with MB61⁰ and MB61²²² isolates. (A) Hierarchical clustering of average protein lists from NI Calu-3 cells and Calu-3 cells infected with SARS-CoV-2 MB61⁰ or MB61²²² isolates, collected at 12, 24, and 48 h p.i. The dendrogram was obtained by computing the average PSMs of DEPs selected by LDA; Euclidean's distance metric and Ward's methods were applied. Categories were reported in different colors accordingly to the isolates and time p.i. (B) and (C) Histograms DEP trend in the major pathways involved at 48 h p.i. comparing MB61⁰ versus MB61²²² isolates. Orange bars and negative DAve values refer to upregulated proteins in MB61²²², whereas light blue bars and positive DAve values refer to upregulated proteins in MB61⁰. For each protein, gene name and related DAve value (ratio of protein expression) are reported.

escape. In particular, they discovered an upregulation of N, N*, and Orf9b expression in Alpha (B.1.1.7) variant. These proteins, encoded by the N alternative reading frame, are key viral innate antagonists. They suppose that the increase in Orf9b transcription derives from one-base deletion at 28,271 found in Alpha and Delta (B.1.617.2) variants and A > T substitution in the Omicron (B.1.1.529) variant, which weakens their Kozak translation initiation complex enhancing leaky scanning of the N gene. Additionally, an increase in Orf9b protein expression is likely influenced by 3-nucleotide mutation at 28,280–28,282 GAT > CTA,

which modifies the Alpha Orf9b Kozak context introducing an enhanced transcriptional regulatory sequence (TRS). We evaluated MB61⁰ and MB61²²² N gene sequences but, as shown in Supplementary Fig. S7, we did not detect any of the above-described nucleotide changes, thus excluding their role in establishing different innate immune responses evoked by the two isolates.

It has been previously suggested (Parker et al. 2021) that the 3-nucleotide mutation at 28,881–28,883 GGG > AAC found in Alpha, Gamma, and Omicron variants creates a novel TRS for N* transcription. Increased N* protein levels are

supposed to act as innate immune antagonists by sequestering double-stranded RNA. However, this mechanism cannot explain the different capabilities of our isolates to trigger innate immunity since both MB61[0] and MB61[222] show these nucleotide changes in their *N* gene sequence (Supplementary Fig. S7).

Interestingly, coinfection of two human cell lines of different origin with our two SARS-CoV-2 isolates highlighted the dramatic predominance of MB61[222] replication over that of MB61[0]. This may be attributed to a faster replication activity of MB61[222] compared to MB61[0] and to the capability of MB61[222] to activate RNA sensors and trigger potent innate immune responses. IFN-stimulated gene products are involved in SARS-CoV-2 entry steps, as IFITMs (Shi et al. 2021; Winstone et al. 2021). Four members of these proteins (IFITM1, IFITM2, IFITM3, and IFITM5) are strongly induced by type-I and type-II IFNs and are known to act as antiviral molecules against Influenza A viruses, Flaviviruses, Filoviruses, and SARS-CoV (Szabo and Bugge 2008, 2011). More recently, IFITM2 was found to restrict SARS-CoV-2 entry that occurs by endocytosis (Winstone et al. 2021). Although the mechanisms are still unknown, IFITM2 was found to prevent SARS-CoV-2 from traversing the endosomal membrane to access the cellular cytoplasm. Interestingly, this did not occur if SARS-CoV-2 gains access to the target cells by fusion at the PM (Huang et al. 2011). We observed an increased expression of IFITM1 and IFITM2 during MB61[222] infection, suggesting a possible implication of IFITMs in selectively impairing MB61[0] replication. Indeed, the ability of MB61[222] to shift viral entry toward the PM fusion pathway may allow it to escape the host cell blocking of endosomal viral entry. On the contrary, MB61[0] is a target for the antiviral activity of IFITM1 and IFITM2 because it lacks the possibility to use the PM fusion pathway. These findings suggest that during coinfection of a cell with the two SARS-CoV-2 isolates, MB61[222] may dominate by triggering an IFN-mediated activity aimed to neutralize MB61[0] entry and replication.

MB61[222] is able to evoke a potent innate immune response, which consists in the production and release of type-I and -II IFNs and different proinflammatory cytokines. Usually, early host innate responses protect airway cells from infection and limit viral dissemination (Sposito et al. 2021). The capability of MB61[222] to actively replicate in such an unfavorable microenvironment supports the hypothesis that it can escape host innate responses by activating still unknown antagonists. Indeed, viral innate resistance is likely to have contributed to prolonged *in vivo* viral shedding in the immunocompromised host, whose antiviral defenses were essentially based on innate immunity. This hypothesis is also consistent with reports of enhanced innate evasion and prolonged shedding of the Alpha variant (Calistri et al. 2021; Kissler et al. 2021; Thorne et al. 2021). It is worth noting that the inflammatory switch operated by MB61[222] may have evolved to also enhance viral spreading at the site of infection as already evidenced for the Alpha variant (Davies et al. 2021; Scientific Advisory Group for Emergencies 2021). Altogether, our findings highlight the importance of innate immune evasion in the still ongoing process of SARS-CoV-2 evolution aimed to find the optimal adaptation to replicate and disseminate into the human host. However, the role of other mutations than N501T and Q493K acquired by MB61[222], in increasing viral replication, promoting innate immune evasion, and changing the cytokine profile, cannot be completely ruled out.

In conclusion, this study further points to uncontrolled and prolonged infection in immunocompromised patients as the condition that may have shaped the emergence of SARS-CoV-2 variants with a higher capability than their ancestors to rapidly spread around the world. Interestingly, our data show competition among virus quasispecies to hold a dominant replicative activity and spread by manipulating the host cell's innate immunity. This finding subverts the idea of quasispecies as an advantage mutation pool for the epidemic variants to find the best genetic fitness during intra-host evolution and introduces a new concept of quasispecies fighting for host dominance by taking benefit from the cell machinery to restrict the productive infection of the other competitors in the viral ensemble. This may explain, at least in part, the extraordinary rapid worldwide turnover of a VOC over the original pandemic strain observed in the COVID-19 pandemic. The preexistence of potential fitness mutants calls for the importance of studying the mutation spectra of different hosts and minor mutants in particular, to predict the emergence of new variants with neutralizing antibody or antiviral drug escape ability.

Data availability

Supplementary data

Supplementary data is available at *Virus Evolution* online.

Funding

Conflict of interest: The authors declare no conflict of interest.

References

Abdul-Jawad, S. et al. (2021) 'Acute Immune Signatures and Their Legacies in Severe Acute Respiratory Syndrome Coronavirus-2 Infected Cancer Patients', *Cancer Cell*, 39: 257–75.e6.

Al Khatib, H. A. et al. (2020) 'Within-Host Diversity of SARS-CoV-2 in COVID-19 Patients with Variable Disease Severities', *Frontiers in Cellular and Infection Microbiology*, 10: 575613.

Al-Saleem, J. et al. (2019) 'HTLV-1 Tax-1 Interacts with SNX27 to Regulate Cellular Localization of the HTLV-1 Receptor Molecule, GLUT1', *PLoS One*, 14: e0214059.

Alteri, C. et al. (2021) 'Genomic Epidemiology of SARS-CoV-2 Reveals Multiple Lineages and Early Spread of SARS-CoV-2 Infections in Lombardy, Italy', *Nature Communication*, 12: 434.

Arslan, A. D. (2017) 'Human SLFN5 Is a Transcriptional Co-repressor of STAT1-mediated Interferon Responses and Promotes the Malignant Phenotype in Glioblastoma', *Oncogene*, 36: 6006–19.

Avanzato, V. A. et al. (2020) 'Case Study: Prolonged Infectious SARS-CoV-2 Shedding from an Asymptomatic Immunocompromised Individual with Cancer', *Cell*, 183: 1901–12.e9.

Baang, J. H. et al. (2021) 'Prolonged Severe Acute Respiratory Syndrome Coronavirus 2 Replication in an Immunocompromised Patient', *The Journal of Infectious Diseases*, 223: 23–7.

Bayarri-Olmos, R. et al. (2021) 'The alpha/B.1.1.7 SARS-CoV-2 Variant Exhibits Significantly Higher Affinity for ACE-2 and Requires Lower Inoculation Doses to Cause Disease in K18-hACE2 Mice', *Elife*, 10: e70002.

Bortolotti, D. et al. (2020) 'SARS-CoV-2 Spike 1 Protein Controls Natural Killer Cell Activation via the HLA-E/NKG2A Pathway', *Cells*, 9: 1975.

——— et al. (2021) 'TLR3 and TLR7 RNA Sensor Activation during SARS-CoV-2 Infection', *Microorganisms*, 9: 1820.

Caccuri, F. et al. (2020) 'A Persistently Replicating SARS-CoV-2 Variant Derived from an Asymptomatic Individual', *Journal of Translational Medicine*, 18: 362.

——— et al. (2021) 'SARS-CoV-2 Infection Remodels the Phenotype and Promotes Angiogenesis of Primary Human Lung Endothelial Cells', *Microorganisms*, 9: 1438.

Calistri, P. et al. (2021) 'Infection Sustained by Lineage B.1.1.7 Of SARS-CoV-2 Is Characterised by Longer Persistence and Higher Viral RNA Loads in Nasopharyngeal Swabs', *International Journal of Infectious Diseases*, 105: 753–5.

Camprubí, D. et al. (2020) 'Persistent Replication of SARS-CoV-2 in a Severely Immunocompromised Patient Treated with Several Courses of Remdesivir', *International Journal of Infectious Diseases: IJID: Official Publication of the International Society for Infectious Diseases*, 104: 379–81.

Caruso, A. et al. (2021) 'Methotrexate Inhibits SARS-CoV-2 Virus Replication "in vitro"', *Journal of Medical Virology*, 93: 1780–5.

Case, D. A. et al. (2018) *Amber 2018*. University of California: San Francisco, CA, USA.

Cevik, M. et al. (2021) 'SARS-CoV-2, SARS-CoV, and MERS-CoV Viral Load Dynamics, Duration of Viral Shedding, and Infectiousness: A Systematic Review and Meta-analysis', *Lancet Microbe*, 2: e13–22.

Challen, R. et al. (2021) 'Risk of Mortality in Patients Infected with SARS-CoV-2 Variant of Concern 202012/1: Matched Cohort Study', *BMJ*, 372: n579.

Chen, C. Y., and Brodsky, F. M. (2005) 'Huntingtin-interacting Protein 1 (Hip1) and Hip1-related Protein (Hip1r) Bind the Conserved Sequence of Clathrin Light Chains and Thereby Influence Clathrin Assembly in Vitro and Actin Distribution in Vivo', *Journal of Biological Chemistry*, 280: 6109–17.

Choi, B. et al. (2020) 'Persistence and Evolution of SARS-CoV-2 in an Immunocompromised Host', *The New England Journal of Medicine*, 383: 2291–3.

Davies, N. G. et al. (2021) 'Increased Mortality in Community-tested Cases of SARS-CoV-2 Lineage B.1.1.7', *Nature*, 593: 270–4.

Dhar, M. S. et al. (2021) 'Genomic Characterization and Epidemiology of an Emerging SARS-CoV-2 Variant in Delhi, India', *Science*, 374: 995–9.

Di Silvestre, D. et al. (2013) 'Multidimensional Protein Identification Technology for Direct-tissue Proteomics of Heart', *Methods in Molecular Biology*, 2005: 25–38.

Domingo, E. et al. (2021) 'Historical Perspective on the Discovery of the Quasispecies Concept', *Annual Review of Virology*, 23: 3–20.

Doncheva, N. T. et al. (2019) 'Cytoscape StringApp: Network Analysis and Visualization of Proteomics Data', *Journal of Proteome Research*, 18: 623–32.

ECDC. (2020), *Rapid Increase of a SARS-CoV-2 Variant with Multiple Spike Protein Mutations Observed in the United Kingdom* <https://www.ecdc.europa.eu/sites/default/files/documents/SARS-CoV-2-variant-multiple-spike-protein-mutations-United-Kingdom.pdf> accessed 2 Feb 2022.

Faria, N. R. et al. (2021) 'Genomics and Epidemiology of the P.1 SARS-CoV-2 Lineage in Manaus, Brazil', *Science*, 372: 815–21.

Fiorentini, S. et al. (2021) 'First Detection of SARS-CoV-2 Spike Protein N501 Mutation in Italy in August, 2020', *The Lancet Infectious Diseases*, 21: e147.

Griffin, N. M. et al. (2010) 'Label-free, Normalized Quantification of Complex Mass Spectrometry Data for Proteomic Analysis', *Nature Biotechnology*, 28: 83–9.

Hensley, M. K. et al. (2021) 'Intractable Coronavirus Disease 2019 (COVID-19) and Prolonged Severe Acute Respiratory Syndrome Coronavirus 2 (SARS-CoV-2) Replication in A Chimeric Antigen Receptor-Modified T-Cell Therapy Recipient: A Case Study', *Clinical Infectious Diseases: An Official Publication of the Infectious Diseases Society of America*, 73: e815–21.

Huang, I. C. et al. (2011) 'Distinct Patterns of IFITM-mediated Restriction of Filoviruses, SARS Coronavirus, and Influenza A Virus', *PLoS Pathogens*, 7: e1001258.

Jackson, C. B. et al. (2022) 'Mechanisms of SARS-CoV-2 Entry into Cells', *Nature Reviews. Molecular Cell Biology*, 23: 3–20.

Jurrus, E. et al. (2018) 'Improvements to the APBS Biomolecular Solvation Software Suite', *Protein Science*, 27: 112–28.

Käll, L. et al. (2007) 'Semi-supervised Learning for Peptide Identification from Shotgun Proteomics Datasets', *Nature Methods*, 4: 923–5.

Kang, H. et al. (2020) 'Retest Positive for SARS-CoV-2 RNA of "recovered" Patients with COVID-19: Persistence, Sampling Issues, or Re-infection?' *Journal of Medical Virology*, 92: 2263–5.

Kemp, S. A. et al. (2020) 'Neutralising Antibodies in Spike Mediated SARS-CoV-2 Adaptation', *medRxiv*, 2020: 2020. 12.05.20241927.

Kissler, S. M. et al. (2021) 'Densely Sampled Viral Trajectories Suggest Longer Duration of Acute Infection with B. 1.1. 7 Variant Relative to non-B. 1.1. 7 SARS-CoV-2', *medRxiv*.

Krissinel, E., and Henrick, K. (2007) 'Inference of Macromolecular Assemblies from Crystalline State', *Journal of Molecular Biology*, 372: 774–97.

Laferl, H. et al. (2021) 'An Approach to Lifting Self-isolation for Health Care Workers with Prolonged Shedding of SARS-CoV-2 RNA', *Infection*, 49: 95–101.

Larrson, A. (2014) 'AliView: A Fast and Lightweight Alignment Viewer and Editor for Large Data Sets', *Bioinformatics*, 30: 3276–8.

Lee, S. et al. (2020) 'Clinical Course and Molecular Viral Shedding among Asymptomatic and Symptomatic Patients with SARS-CoV-2 Infection in a Community Treatment Center in the Republic of Korea', *JAMA Internal Medicine*, 180: 1–6.

Li, C. et al. (2020) 'Highly Sensitive and Full-genome Interrogation of SARS-CoV-2 Using Multiplexed PCR Enrichment Followed by Next-generation Sequencing', *bioRXiv*.

Liu, H. et al. (2021) 'The Basis of a More Contagious 501Y.V1 Variant of SARS-CoV-2', *Cell Research*, 31: 720–2.

Liu, T. et al.) (2017) 'NF-κB Signaling in Inflammation', *Signal Transduction and Targeted Therapy*, 2017: 17023.

Lythgoe, K. A. et al. (2021) 'SARS-CoV-2 within-Host Diversity and Transmission', *Science*, 372: eabg0821.

Madden, E. et al. (2019) 'The Role of the Unfolded Protein Response in Cancer Progression: From Oncogenesis to Chemoresistance', *Biology of the Cell*, 111: 1–17.

Maere, S. et al. (2005) 'BiNGO: A Cytoscape Plugin to Assess Overrepresentation of Gene Ontology Categories in Biological Networks', *Bioinformatics*, 21: 3448–9.

Mdkhana, B. et al. (2021) 'Nucleic Acid-Sensing Pathways during SARS-CoV-2 Infection: Expectations versus Reality', *Journal of Inflammation Research*, 14: 199–216.

Minh, B. Q. et al. (2020) 'IQ-TREE 2: New Models and Efficient Methods for Phylogenetic Inference in the Genomic Era', *Molecular Biology Evolution*, 1: 37.

Nakamura, T. et al. (2018) 'Parallelization of MAFFT for Large-scale Multiple Sequence Alignments', *Bioinformatics*, 34: 2490–2.

Nelson, G. et al. (2021) 'Molecular Dynamic Simulation Reveals E484K Mutation Enhances Spike RBD-ACE2 Affinity and the Combination of E484K, K417N and N501Y Mutations (501Y.V2 Variant) Induces Conformational Change Greater than N501Y Mutant Alone, Po Tentially Resulting in an Escape Mutant', *bioRxiv*.

Nguyen, H. et al. (2020) 'A Role of Intracellular Toll-Like Receptors (3, 7, and 9) in Response to Mycobacterium Tuberculosis and Co-Infection with HIV 1', *International Journal of Molecular Sciences*, 21: 6148.

O'Sullivan, E. D. et al. (2020) 'Prolonged SARS-CoV-2 Viral Shedding in Patients with Chronic Kidney Disease', *Nephrology*, 26: 328–32.

O'Toole, A. et al. (2021) 'Assignment of Epidemiological Lineages in an Emerging Pandemic Using the Pangolin Tool', *Virus Evolution*, 7: veab064.

Parker, M. D. et al. (2021) 'Altered Subgenomic RNA Expression in SARS-CoV-2 B.1.1.7 Infections', *bioRxiv*.

Passamonti, F. et al. (2020) 'Clinical Characteristics and Risk Factors Associated with COVID-19 Severity in Patients with Haematological Malignancies in Italy: A Retrospective, Multicentre, Cohort Study', *Lancet Haematology*, 7: e737–45.

Pfaender, S. et al. (2020) 'LY6E Impairs Coronavirus Fusion and Confers Immune Control of Viral Disease', *Nature Microbiology*, 5: 1330–9.

Piovesan, D. et al. (2016) 'The RING 2.0 Web Server for High Quality Residue Interaction Networks', *Nucleic Acids Research*, 44: W367–74.

Racki, N. et al. (2014) 'Reverse Transcriptase Droplet Digital PCR Shows High Resilience to PCR Inhibitors from Plant, Soil and Water Samples', *Plant Methods*, 10: 42.

Ramanathan, M. et al. (2021) 'SARS-CoV-2 B.1.1.7 And B.1.351 Spike Variants Bind Human ACE2 with Increased Affinity', *The Lancet Infectious Diseases*, 21: 1070.

Sagulenko, P. et al. (2018) 'TreeTime: Maximum-likelihood Phylodynamic Analysis', *Virus Evol*, 4: vex042.

Schmitz, M. L. et al. (2014) 'The Intricate Interplay between RNA Viruses and NF-κB', *Biochimica Et Biophysica Acta (BBA) - Molecular Cell Research*, 1843: 2754–64.

Scientific Advisory Group for Emergencies. (2021), *NERVTAG: Update Note on B.1.1.7 Severity*. UK government <https://assets.publishing.service.gov.uk/government/uploads/system/uploads/attachment_data/file/982640/Feb_NERVTAG_update_note_on_B.1.1.7_severity.pdf> accessed Feb 2021.

Shi, G. et al. (2021) 'Opposing Activities of IFITM Proteins in SARS-CoV-2 Infection', *EMBO Journal*, 40: e106501.

Siqueira, J. D. et al. (2021) 'Distinguishing SARS-CoV-2 Bonafide Re-Infection from Pre-Existing Minor Variant Reactivation', *Infection, Genetics and Evolution: Journal of Molecular Epidemiology and Evolutionary Genetics in Infectious Diseases*, 90: 104772.

Snijder, E. J. et al. (2020) 'A Unifying Structural and Functional Model of the Coronavirus Replication Organelle: Tracking down RNA Synthesis', *PLoS Biology*, 18: e3000715.

Sposito, B. et al. (2021) 'The Interferon Landscape along the Respiratory Tract Impacts the Severity of COVID-19', *Cell*, 184: 4953–68e16.

Stanton, B. A. (2020) 'SARS-CoV-2 (COVID-19) and Cystic Fibrosis', *American Journal of Physiology*, 319: L408–15.

Starr, T. N. et al. (2020) 'Deep Mutational Scanning of SARS-CoV-2 Receptor Binding Domain Reveals Constraints on Folding and ACE2 Binding', *Cell*, 182: 1295–310.e20.

Su, G. et al. (2014) 'Biological Network Exploration with Cytoscape 3', *Current Protocols in Bioinformatics*, 47: 8.13.1–24.

Sun, F. et al. (2021) 'SARS-CoV-2 Quasispecies Provides an Advantage Mutation Pool for the Epidemic Variants', *Microbiology Spectrum*, 9: e0026121.

Szabo, R., and Bugge, T. H. (2008) 'Type II Transmembrane Serine Proteases in Development and Disease', *The International Journal of Biochemistry & Cell Biology*, 40: 1297–316.

——— (2011) 'Membrane-anchored Serine Proteases in Vertebrate Cell and Developmental Biology', *Annual Review of Cell and Developmental Biology*, 27: 213–35.

Tang, W. et al. (2011) 'The Growth Factor Progranulin Binds to TNF Receptors and Is Therapeutic against Inflammatory Arthritis in Mice', *Science*, 332: 478–4.

Tegally, H. et al. (2021) 'Detection of a SARS-CoV-2 Variant of Concern in South Africa', *Nature*, 592: 438–43.

Thomson, E. C. et al. (2021) 'Circulating SARS-CoV-2 Spike N439K Variants Maintain Fitness while Evading Antibody-mediated Immunity', *Cell*, 184: 1171–87.

Thorne, L. G. et al. (2021) 'Evolution of Enhanced Innate Immune Evasion by SARS-CoV-2', *Nature*, 602: 487–95.

Tian, F. et al. (2021) 'N501Y Mutation of Spike Protein in SARS-CoV-2 Strengthens Its Binding to Receptor ACE2', *Elife*, 10: e69091.

Valesano, A. L. et al. (2021) 'Temporal Dynamics of SARS-CoV-2 Mutation Accumulation within and across Infected Hosts', *PLoS Pathogens*, 17: e1009499.

Vercauteren, D. et al. (2010) 'The Use of Inhibitors to Study Endocytic Pathways of Gene Carriers: Optimization and Pitfalls', *Molecular Therapy*, 18: 561–9.

Viana, R. et al. (2022) 'Rapid Epidemic Expansion of the SARS-CoV-2 Omicron Variant in Southern Africa', *Nature*, 603: 679–86.

Vijenthira, A. et al. (2020) 'Outcomes of Patients with Hematologic Malignancies and COVID-19: A Systematic Review and Meta-analysis of 3377 Patients', *Blood*, 136: 2881–92.

Vladimer, G. I. et al. (2014) 'IFITs: Emerging Roles as Key Anti-viral Proteins', *Frontiers in Immunology*, 5: 94.

Voloch, C. M. et al. (2021) 'Intra-host Evolution during SARS-CoV-2 Prolonged Infection', *Virus Evolution*, 7: 1–11.

Wang, D. et al. (2021a) 'Population Bottlenecks and Intra-Host Evolution during Human-to-Human Transmission of SARS-CoV-2', *Frontiers of Medicine*, 8: 585358.

Wang, Y. et al. (2021b) 'Intra-Host Variation and Evolutionary Dynamics of SARS-CoV-2 Populations in COVID-19 Patients', *Genome Medicine*, 13: 30.

Waterhouse, A. et al. (2018) 'SWISS-MODEL: Homology Modelling of Protein Structures and Complexes', *Nucleic Acids Research*, 46: W296–303.

Wei, Y. et al. (2017) 'CD59 Association with Infectious Bronchitis Virus Particles Protects against Antibody-dependent Complement-mediated Lysis', *Journal of General Virology*, 98: 2725–30.

Wilkinson, E. et al. (2021) 'A Year of Genomic Surveillance Reveals How the SARS-CoV-2 Pandemic Unfolded in Africa', *Science*, 374: 423–31.

Winstone, H. et al. (2021) 'The Polybasic Cleavage Site in SARS-CoV-2 Spike Modulates Viral Sensitivity to Type I Interferon and IFITM2', *Journal of Virology*, 95: e02422–20.

Wu, F. et al. (2020) 'A New Coronavirus Associated with Human Respiratory Disease in China', *Nature*, 579: 265–9.

Yanai, H. et al. (2018) 'Revisiting the Role of IRF3 in Inflammation and Immunity by Conditional and Specifically Targeted Gene Ablation in Mice', *Proceedings of the National Academy of Sciences of the United States of America (PNAS USA)*, 115: 5253–8.

Zapor, M. (2020) 'Persistent Detection and Infectious Potential of SARS-CoV-2 Virus in Clinical Specimens from COVID-19 Patients', *Viruses*, 12: 1384.

Zhou, P. et al. (2020) 'A Pneumonia Outbreak Associated with A New Coronavirus of Probable Bat Origin', *Nature*, 579: 270–3.